



TEMPOEST: a Bayesian approach to pulsar timing analysis

L. Lentati,¹★ P. Alexander,¹ M. P. Hobson,¹ F. Feroz,¹ R. van Haasteren,² K. J. Lee³ and R. M. Shannon⁴

¹Astrophysics Group, Cavendish Laboratory, JJ Thomson Avenue, Cambridge CB3 0HE, UK

²Max-Planck-Institut für Gravitationsphysik (Albert-Einstein-Institut), D-30167 Hannover, Germany

³Max-Planck-Institut für Radioastronomie, Auf dem Hugel 69, D-53121 Bonn, Germany

⁴CSIRO Astronomy and Space Science, Australia Telescope National Facility, Box 76 Epping, NSW 1710, Australia

Accepted 2013 November 1. Received 2013 October 30; in original form 2013 August 6

ABSTRACT

A new Bayesian software package for the analysis of pulsar timing data is presented in the form of TEMPOEST which allows for the robust determination of the non-linear pulsar timing solution simultaneously with a range of additional stochastic parameters. This includes both red spin noise and dispersion measure variations using either power-law descriptions of the noise, or through a model-independent method that parametrizes the power at individual frequencies in the signal. We use TEMPOEST to show that at noise levels representative of current data sets in the European Pulsar Timing Array and International Pulsar Timing Array the linear timing model can underestimate the uncertainties of the timing solution by up to an order of magnitude. We also show how to perform Bayesian model selection between different sets of timing model and stochastic parameters, for example, by demonstrating that in the pulsar B1937+21 both the dispersion measure variations and spin noise in the data are optimally modelled by simple power laws. Finally, we show that not including the stochastic parameters simultaneously with the timing model can lead to unpredictable variation in the estimated uncertainties, compromising the robustness of the scientific results extracted from such analysis.

Key words: methods: data analysis – pulsars: general – pulsars: individual: B1937+21.

1 INTRODUCTION

The ever increasing precision of pulsar timing studies, combined, in particular, with the exceptional rotational stability of millisecond pulsars (MSPs) has resulted in a powerful tool for the pursuit of a wide range of scientific goals. For example, in recent years pulsar timing has been used to find extrasolar planets (Bailes et al. 2011), to study matter at super-nuclear densities in the interior of neutron stars (Espinoza et al. 2011), and in the double pulsar system PSR J0737–3039A/B, provides precise measurements of several ‘post-Keplerian’ parameters allowing for stringent tests of general relativity (Kramer et al. 2006).

For a detailed review of pulsar timing refer to e.g. Lorimer et al. (2004). In brief, the arrival times of pulses (TOAs) for a particular pulsar will be recorded by an observatory in a series of discrete observations over a period of time. These arrival times must all be transformed into a common frame of reference, the Solar system barycentre, in order to correct for the motion of the Earth.

A model for the pulsar can then be fitted to the TOAs that characterizes the properties of the pulsar’s orbital motion, as well as its timing properties such as its orbital frequency and spin down. This is most commonly carried out using the TEMPO,¹ and more recently, TEMPO2 pulsar timing packages (Hobbs, Edwards & Manchester 2006; Edwards, Hobbs, & Manchester 2006; Hobbs et al. 2009). TEMPO2 uses an initial guess of the timing model to generate a set of pre-fitting residuals. A Fisher-matrix approximation to the timing model parameters is then calculated and a linear least-squares method is utilized to improve the fit. If desired, multiple iterations can be performed such that the best-fitting values for the timing model from the previous iteration are used as the starting guess for the next, until convergence is reached.

When performing this fitting process, TEMPO2 considers the TOAs to be solely the sum of a deterministic signal due to the timing model, and a white noise component described completely by the TOA uncertainties. In realistic data sets however this assumption is rarely true. If additional stochastic processes, such as intrinsic red spin noise due to rotational irregularities in the neutron star

* E-mail: tl21@cam.ac.uk

¹ <http://www.atnf.csiro.au/research/pulsar/tempo>

(Shannon & Cordes 2010) or correlated noise due to a stochastic gravitational wave background (GWB) generated by, for example, coalescing black holes (e.g. Phinney 2001; Jaffe & Backer 2003), are present in the data, then power from these contributions will be absorbed by the timing model, affecting the accuracy of the parameter estimation.

Recently, Coles et al. (2011, henceforth C11) proposed a method of improving the timing model fit by using the Cholesky-decomposition of the covariance matrix describing the properties of these additional stochastic processes in the TOAs, calculated from the power spectral density of the timing residuals. This can be used to whiten the residuals, after which parameter estimation is performed in these transformed observations using ordinary least squares.

In van Haasteren & Levin (2013, henceforth vHL2013), however, it is shown that after fitting for the timing model the resulting residuals are not time stationary, and as such the power spectral density of those residuals is not a well-defined mathematical quantity. In addition, because the method in C11 does not account for the covariance between the timing model and the stochastic processes, the uncertainties associated with the parameter estimates, in particular those associated with the quadratic spin down, are not optimal. The preferred approach is therefore to perform a joint analysis of the deterministic timing model and any additional stochastic components present as in vHL2013.

However, when performing a Bayesian analysis using the linearized timing model as presented in vHL2013, it is not possible to perform model selection between different sets of timing model parameters using the evidence. This is because the maximum likelihood value at which the linearization is performed will depend upon the exact set of model parameters included, and as such, both the data and the model will vary as the parameter space changes. It is also not clear how the estimation of the uncertainties of the timing model parameters depends on the linearization process, especially in the regime where the signal-to-noise ratio might be low, and the Fisher-matrix approximation will be poor.

In this paper, we present a solution to these problems in the form of TEMPONEST. TEMPONEST provides a means of performing a simultaneous analysis of either the linear or non-linear timing model and additional stochastic parameters using the Bayesian inference tool MULTINEST (Feroz & Hobson 2008; Feroz, Hobson & Bridges 2009) to efficiently explore this joint parameter space, whilst using TEMPO2 as an established means of evaluating the timing model at each point in that space. TEMPONEST allows for robust model selection between different sets of timing model or noise parameters, and requires only basic prior knowledge of the timing model.

In Section 2, we will describe the basic principles of our Bayesian approach to data analysis, giving a brief overview of how it may be used to perform model selection, and introduce MULTINEST. In Section 3, we will describe the stochastic models currently available for use in TEMPONEST to include with the timing model, including the white noise modifiers EFAC and EQUAD, along with descriptions of both red spin noise and dispersion measure (DM) variations.

We will then perform a series of tests using TEMPONEST designed to show some of the included functionality. In Section 6, we use simulated data to compare the non-linear and linear approximation to the timing model across different noise regimes designed to represent both future and current data sets, whilst in Section 7, we apply TEMPONEST to two sets of publicly available data, first of the binary pulsar B1855+09 and then the isolated pulsar B1937+21. We show how TEMPONEST can be used to perform Bayesian model selection between different sets of timing model and stochastic

parameters, and for the latter case, also compare the parameters estimates and uncertainties for the timing solutions produced by TEMPONEST, TEMPO2 and the SpectralModel plug-in for TEMPO2 that uses the principles described in C11.

We note that the aim of this paper is not to provide a user manual for TEMPONEST, but rather give an overview of its functionality. A development build of TEMPONEST is currently available online,² with a full public release planned in the near future.

This research is the result of the common effort to directly detect gravitational waves using pulsar timing, known as the European Pulsar Timing Array (Janssen et al. 2008).³

2 BAYESIAN INFERENCE

Our method for performing pulsar timing analysis is built upon the principles of Bayesian inference, which provides a consistent approach to the estimation of a set of parameters Θ in a model or hypothesis H given the data, D . Bayes' theorem states that

$$\Pr(\Theta | D, H) = \frac{\Pr(D | \Theta, H)\Pr(\Theta | H)}{\Pr(D | H)}, \quad (1)$$

where $\Pr(\Theta | D, H) \equiv \Pr(\Theta)$ is the posterior probability distribution of the parameters, $\Pr(D | \Theta, H) \equiv L(\Theta)$ is the likelihood, $\Pr(\Theta | H) \equiv \pi(\Theta)$ is the prior probability distribution and $\Pr(D | H) \equiv Z$ is the Bayesian evidence.

In parameter estimation, the normalizing evidence factor is usually ignored, since it is independent of the parameters Θ . Inferences are therefore obtained by taking samples from the (unnormalized) posterior using, for example, standard Markov chain Monte Carlo sampling methods.

In contrast to parameter estimation, for model selection the evidence takes the central role and is simply the factor required to normalize the posterior over Θ :

$$Z = \int L(\Theta)\pi(\Theta)d^n\Theta, \quad (2)$$

where n is the dimensionality of the parameter space.

As the average of the likelihood over the prior, the evidence is larger for a model if more of its parameter space is likely and smaller for a model where large areas of its parameter space have low likelihood values, even if the likelihood function is very highly peaked. Thus, the evidence automatically implements Occam's razor: a simpler theory with a compact parameter space will have larger evidence than a more complicated one, unless the latter is significantly better at explaining the data.

The question of model selection between two models H_0 and H_1 can then be decided by comparing their respective posterior probabilities, given the observed data set D , via the model selection ratio R :

$$R = \frac{P(H_1 | D)}{P(H_0 | D)} = \frac{P(D | H_1)P(H_1)}{P(D | H_0)P(H_0)} = \frac{Z_1}{Z_0} \frac{P(H_1)}{P(H_0)}, \quad (3)$$

where $P(H_1)/P(H_0)$ is the a priori probability ratio for the two models, which can often be set to unity but occasionally requires further consideration.

² <https://github.com/LindleyLentati/TempoNest>

³ [www.epta.eu.org/](http://epta.eu.org/)

2.1 Nested sampling and evaluating the evidence

Evaluation of the multidimensional integral in equation (2) is a challenging numerical task. Standard techniques like thermodynamic integration (O’Rourke & Fitzgerald 1996) are extremely computationally expensive, which makes evidence evaluation at least an order-of-magnitude more costly than parameter estimation. Some fast approximate methods have been used for evidence evaluation, such as treating the posterior as a multivariate Gaussian centred at its peak (see e.g. Hobson, Bridle & Lahav 2002), but this approximation is clearly a poor one for multimodal posteriors (except perhaps if one performs a separate Gaussian approximation at each mode). The Savage–Dickey density ratio has also been proposed (see e.g. Trotta 2007) as an exact, and potentially faster, means of evaluating evidences, but is restricted to the special case of nested hypotheses and a separable prior on the model parameters.

The nested sampling approach (Skilling 2004) is a Monte Carlo method targeted at the efficient calculation of the evidence, but also produces posterior inferences as a by-product.

Nested sampling considers the prior volume X where the likelihood is greater than some value λ , which can be written as

$$X(\lambda) = \int_{L(\Theta) > \lambda} \pi(\Theta) d^n \Theta. \quad (4)$$

This allows us to rewrite equation (2) as a one-dimensional integral over λ :

$$Z = \int_0^\infty X(\lambda) d\lambda. \quad (5)$$

When the inverse of $X(\lambda)$, the likelihood value that corresponds to a given prior volume, $L(X)$, exists, this integral can then be written as

$$Z = \int_0^1 L(X) dX, \quad (6)$$

and so the evidence can be calculated as the weighted sum of a set of M values of X :

$$Z = \sum_{i=1}^M L_i w_i, \quad (7)$$

where the weights w_i are simply given by the trapezium rule $w_i = \frac{1}{2}(X_{i-1} - X_{i+1})$.

2.2 MULTINEST

In Feroz et al. (2009) and Feroz & Hobson (2008), this nested sampling framework was built upon with the introduction of the MULTINEST algorithm, which provides an efficient means of sampling from posteriors that may contain multiple modes and/or large (curving) degeneracies, and also calculates the evidence. Since its release MULTINEST has been used successfully in a wide range of astrophysical problems, from detecting the Sunyaev–Zel’dovich effect in galaxy clusters (AMI Consortium et al. 2012), to inferring the properties of a potential stochastic GWB in pulsar timing array data (Lentati et al. 2013, henceforth L13).

In brief, the MULTINEST algorithm operates by first drawing a set of N_{live} points from the prior $\pi(\Theta)$. An ellipsoidal decomposition is then performed such that the full set of live points is contained within a set of ellipsoids. At each subsequent iteration i a point is drawn with likelihood L from the union of these ellipsoids and is checked to see if it satisfies the constraint $L > L_i$ where L_i is the lowest likelihood value present in the set of live points at that

iteration. If this constraint is satisfied the point replaces the lowest likelihood point in the live set with a probability $1/n_e$ where n_e is the number of ellipsoids in which the new point lies.

In high dimensions, most of the volume in the ellipsoids lies in their outer shells; thus, when the decomposition extends beyond the true isolikelihood surface, the acceptance rate of new points can decrease significantly. In order to maintain high sampling efficiency, in high dimensions MULTINEST therefore contains a ‘constant efficiency’ mode. Here, the total volume enclosed by the ellipsoids is adjusted such that the sampling efficiency meets some user set target. However, whilst this mode is adequate for parameter estimation, the evidence values are not reliable.

Recently, however, the MULTINEST algorithm has been updated to include the concept of importance nested sampling (INS; Cameron & Pettitt 2013), which provides a solution to this problem. Full details can be found in Feroz et al. (2013), but the key difference is that, where with normal nested sampling the rejected points play no further role in the sampling process, INS uses every point sampled to contribute towards the evidence calculation. One outcome of this approach is that even when running in constant efficiency mode the evidence calculated is reliable even in higher (~ 50) dimensional problems.

In pulsar timing analysis, we will often have to deal with timing models that can contain > 20 parameters, which, when combined with the properties of the stochastic component of the signal, can result in a total dimensionality of 50–60. As such, the ability to run in constant efficiency mode whilst still obtaining accurate values for the evidence when these higher dimensional problems arise is crucial in order to perform reliable model selection.

3 PULSAR TIMING LIKELIHOOD

For any pulsar, we can write the TOAs for the pulses as a sum of both a deterministic and a stochastic component:

$$\mathbf{t}_{\text{tot}} = \mathbf{t}_{\text{det}} + \mathbf{t}_{\text{sto}}, \quad (8)$$

where \mathbf{t}_{tot} represents the n TOAs for a single pulsar, with \mathbf{t}_{det} and \mathbf{t}_{sto} the deterministic and stochastic contributions to the total, respectively, where any contributions to the latter will be modelled as random Gaussian processes. Writing the deterministic signal due to the timing model as $\tau(\epsilon)$, and the uncertainty associated with a particular TOA i as σ_i , we can write the likelihood that the data are described solely by the timing model as

$$\Pr(\mathbf{t}|\epsilon) \propto \left(\prod_{i=1}^n \sigma_i^2 \right)^{-1/2} \exp \left(-\frac{1}{2} \sum_{i=1}^n \frac{(t_i - \tau(\epsilon)_i)^2}{\sigma_i^2} \right). \quad (9)$$

This represents the simplest model choice possible in TEMPONEST, including only those free parameters present in the TEMPO2 fit. From here, we can now begin to make our model for the stochastic contribution to the signal more realistic by introducing additional parameters to describe the white and red noise components, in order to compare the evidence with this simpler model and determine the optimal set of parameters supported by the data.

3.1 Additional white noise

When dealing with pulsar timing data, the properties of the white noise can be separated into two components:

- (1) For a given pulsar, each TOA has an associated error bar, the size of which will vary across a set of observations. We can introduce an extra free parameter, denoted EFAC, to account for possible

miscalibration of this radiometer noise (Hobbs et al. 2006). The EFAC parameter therefore acts as a multiplier for all the TOA error bars for a given pulsar, observed with a particular system. TEMPONEST allows for either a single EFAC parameter to be estimated for all TOAs for a given pulsar, or, where the observing system has been flagged for each TOA, a separate EFAC can be included for each system.

(2) A second white noise component is also used to represent some additional source of time independent noise, which we call EQUAD. In principle, this parameter represents something physical about the pulsar, the high-frequency tail of the pulsar's red spin noise power spectrum, or, 'jitter' (Liu et al. 2012), and so should be independent of the observing system. Differences in the integration times between TOAs for different observing epochs can muddy this physical interpretation however, and as such as with EFAC, either a single EQUAD parameter can be estimated for all TOAs for a given pulsar, or for each flagged system separately.

We can therefore rewrite the error σ_i associated with each TOA i as $\hat{\sigma}_i$ so that

$$\hat{\sigma}_i^2 = (\alpha_i \sigma_i)^2 + \beta_i^2, \quad (10)$$

where α and β represent the EFAC and EQUAD parameters applied to TOA i , respectively. Note, this is not how TEMPO2 defines the relationship between the EQUAD and EFAC parameters. Thus, equation (9) can be trivially rewritten to include the new white noise parameters as

$$\Pr(\mathbf{t}|\boldsymbol{\epsilon}, \boldsymbol{\alpha}, \boldsymbol{\beta}) \propto \left(\prod_{i=1}^n \hat{\sigma}_i^2 \right)^{-1/2} \exp \left(-\frac{1}{2} \sum_{i=1}^n \frac{(t_i - \tau(\boldsymbol{\epsilon})_i)^2}{\hat{\sigma}_i^2} \right). \quad (11)$$

3.2 Additional red noise

TEMPONEST currently supports two methods for describing the intrinsic red noise properties of the pulsar: the recently introduced model-independent frequency domain method described in L13 and the power-law model, time domain method described in van Haasteren et al. (2009, henceforth vH2009).

3.2.1 L13 method

We begin by writing the red noise component of the stochastic signal, which we will denote \mathbf{t}_{red} , in terms of its Fourier coefficients \mathbf{a} so that $\mathbf{t}_{\text{red}} = \mathbf{F}\mathbf{a}$ where \mathbf{F} denotes the Fourier transform such that for frequency ν and time t we will have both

$$F_{\nu,t} = \frac{1}{T} \sin(2\pi\nu t), \quad (12)$$

and an equivalent cosine term. Here, T represents the total observing span for the pulsar, and ν the frequency of the signal to be sampled. Defining the number of coefficients to be sampled by n_{\max} , TEMPONEST will then include the set of frequencies with values n/T , where n extends from 1 to n_{\max} . For typical PTA data, Lee et al. (2012) show that a low-frequency cut-off of $1/T$ is sufficient to accurately describe the expected long-term variations present in the data. If necessary though it is also possible to specify arbitrary sets of frequencies such that terms with $\nu \ll 1/T$ can be included in the model, or to allow noise terms where the frequency itself is a free parameter.

For a single pulsar, the covariance matrix φ of the Fourier coefficients \mathbf{a} will be diagonal, with components

$$\varphi_{ij} = \langle a_i a_j^* \rangle = \varphi_i \delta_{ij}, \quad (13)$$

where there is no sum over i , and the set of coefficients $\{\varphi_i\}$ represent the theoretical power spectrum for the residuals.

As discussed in L13, whilst equation (13) states that the Fourier modes are orthogonal to one another, this does not mean that we assume they are orthogonal in the time domain where they are sampled, and it can be shown that this non-orthogonality is accounted for within the likelihood. Instead, in Bayesian terms, equation (13) represents our prior knowledge of the power spectrum coefficients within the data. We are therefore stating that, whilst we do not know the form the power spectrum will take, we know that the underlying Fourier modes are still orthogonal by definition, regardless of how they are sampled in the time domain. It is here then that, should one wish to fit a specific model to the power spectrum coefficients at the point of sampling, such as a broken, or single power law, the set of coefficients $\{\varphi_i\}$ should be given by some function $f(\Theta)$, where we sample from the parameters Θ from which the power spectrum coefficients $\{\varphi_i\}$ can then be derived.

We can then write the joint probability density of the timing model, white noise parameters, power spectrum coefficients and the signal realization, $\Pr(\boldsymbol{\epsilon}, \boldsymbol{\alpha}, \boldsymbol{\beta}, \{\varphi_i\}, \mathbf{a} | \mathbf{t})$, as

$$\begin{aligned} \Pr(\boldsymbol{\epsilon}, \boldsymbol{\alpha}, \boldsymbol{\beta}, \{\varphi_i\}, \mathbf{a} | \mathbf{t}) &\propto \Pr(\mathbf{t} | \boldsymbol{\epsilon}, \boldsymbol{\alpha}, \boldsymbol{\beta}, \mathbf{a}) \\ &\times \Pr(\mathbf{a} | \{\varphi_i\}) \Pr(\{\varphi_i\}). \end{aligned} \quad (14)$$

For our choice of $\Pr(\{\varphi_i\})$, we use an uninformative prior that is uniform in \log_{10} space, and draw our samples from the parameter $\rho_i = \log_{10}(\varphi_i)$ instead of φ_i which has the added advantage that we avoid unnecessary rejections due to samples that have negative coefficients in the sampling process. Given this choice of prior the conditional distributions that make up equation (14) can be written as

$$\begin{aligned} \Pr(\mathbf{t} | \boldsymbol{\epsilon}, \boldsymbol{\alpha}, \boldsymbol{\beta}, \mathbf{a}) &\propto \frac{1}{\sqrt{\det(\mathbf{N})}} \exp \left[-\frac{1}{2} (\mathbf{t} - \boldsymbol{\tau}(\boldsymbol{\epsilon}) - \mathbf{F}\mathbf{a})^T \right. \\ &\quad \left. \times \mathbf{N}^{-1} (\mathbf{t} - \boldsymbol{\tau}(\boldsymbol{\epsilon}) - \mathbf{F}\mathbf{a}) \right] \end{aligned} \quad (15)$$

where $\mathbf{N}_{ij} = \hat{\sigma}_i^2 \delta_{ij}$ and represents the white noise errors in the residuals and

$$\Pr(\mathbf{a} | \{\rho_i\}) \propto \frac{1}{\sqrt{\det \varphi}} \exp \left[-\frac{1}{2} \mathbf{a}^{*T} \varphi^{-1} \mathbf{a} \right]. \quad (16)$$

In TEMPONEST, we then marginalize over all Fourier coefficients \mathbf{a} analytically in order to find the posterior for the remaining parameters alone.

When performing this marginalization, we use a uniform prior for the Fourier coefficients, so that, denoting $\mathbf{t} - \boldsymbol{\tau}(\boldsymbol{\epsilon})$ as $\delta\mathbf{t}$, $(\mathbf{F}^T \mathbf{N}^{-1} \mathbf{F} + \varphi^{-1})$ as Σ and $\mathbf{F}^T \mathbf{N}^{-1} \delta\mathbf{t}$ as \mathbf{d} our marginalized posterior is given by

$$\begin{aligned} \Pr(\boldsymbol{\epsilon}, \boldsymbol{\alpha}, \boldsymbol{\beta}, \{\varphi_i\} | \mathbf{t}) &\propto \frac{\det(\Sigma)^{-1/2}}{\sqrt{\det(\varphi)} \det(\mathbf{N})} \\ &\times \exp \left[-\frac{1}{2} (\delta\mathbf{t}^T \mathbf{N}^{-1} \delta\mathbf{t} - \mathbf{d}^T \Sigma^{-1} \mathbf{d}) \right]. \end{aligned} \quad (17)$$

3.2.2 vH2013 method

Here, we begin by parametrizing the red noise process using a power-law spectral density of the form

$$S(f) = A^2 \left(\frac{f}{1 \text{ yr}^{-1}} \right)^\gamma, \quad (18)$$

where $S(f)$ is the spectral density at frequency f , A is the amplitude of the red noise process and γ is the spectral index. We write the time domain covariance matrix $\mathbf{C}_{ij}^{\text{Red}}$ between observations i and j as given in vH2009:

$$\begin{aligned}\mathbf{C}_{ij}^{\text{Red}} = & \frac{A^2}{f_L^{\gamma-1}} \left\{ \Gamma(1-\gamma) \sin\left(\frac{\pi\gamma}{2}\right) \right. \\ & \times (f_L \tau)^{\gamma-1} - \sum_{n=0}^{\infty} (-1)^n \frac{(f_L \tau)^{2n}}{(2n)!(2n+1-\gamma)} \left. \right\},\end{aligned}\quad (19)$$

where f_L is a low-frequency cut-off and $\tau = 2\pi(t_i - t_j)$ with t_i the i th TOA. In vH2009, it is shown that the quadratic spin down acts to absorb any contribution to the signal that arises from the choice of this low-frequency cut-off, and as such it is only necessary to choose f_L so that $1/f_L$ is much greater than the observing time span in order to obtain rapid convergence of the expression. The result of this however, is that the level of uncertainty in the spin-down parameters will be affected to a much greater extent than any others by the presence of low-frequency stochastic processes in the data, a fact that we will return to in Section 7.2. Finally, denoting the white noise covariance matrix \mathbf{N} as before, we can write the total covariance matrix describing our simulated residuals \mathbf{C}_{ij} as

$$\mathbf{C} = \mathbf{C}^{\text{Red}} + \mathbf{N}. \quad (20)$$

We can then write our likelihood as

$$\begin{aligned}\Pr(\mathbf{t}|\boldsymbol{\epsilon}, \boldsymbol{\alpha}, \beta, A, \gamma) = & \frac{1}{\sqrt{(2\pi)^n \det \mathbf{C}}} \\ & \times \exp\left(-\frac{1}{2}(\mathbf{t} - \boldsymbol{\tau}(\boldsymbol{\epsilon}))^\top \mathbf{C}^{-1}(\mathbf{t} - \boldsymbol{\tau}(\boldsymbol{\epsilon}))\right).\end{aligned}\quad (21)$$

3.3 Including DM variations

The plasma located in the interstellar medium, as well as in solar winds and the ionosphere can result in delays in the propagation of the pulse signal between the pulsar and the observatory, an effect that appears as a red noise signal in the timing residuals.

Unlike other red noise signals however, the severity of the observed DM variations is dependent upon the observing frequency, and as such we can use this additional information to isolate the component of the red noise that results from this effect.

In particular, the group delay $t_g(\nu)$ for a frequency ν is given by the relation

$$t_g(\nu) = \text{DM}/(K\nu^2), \quad (22)$$

where the dispersion constant K is given by

$$K \equiv 2.41 \times 10^{-16} \text{ Hz}^{-2} \text{ cm}^{-3} \text{ pc s}^{-1} \quad (23)$$

and the DM is defined as the integral of the electron density n_e from the Earth to the pulsar:

$$\text{DM} = \int_0^L n_e dl. \quad (24)$$

DM corrections can be included in the analysis as an additional set of stochastic parameters with only minor modifications to the equations (17) and (21) allowing as before, using either a power-law model or the model-independent description. In both cases, we begin by first defining a vector \mathbf{D} of length equal to the number of observations for a given pulsar as

$$D_i = 1/(K\nu_i^2) \quad (25)$$

for observation i with observing frequency ν_i .

3.3.1 Model-independent method

For the model-independent approach, we then need to make a change to our basis vectors such that our DM Fourier modes are described by

$$F_{v,i}^{\text{DM}} = \frac{1}{T} \sin(2\pi\nu_s t_i) D_i \quad (26)$$

and an equivalent cosine term, where T is the length of the observing timespan, and ν_s now explicitly denotes the frequency of the signal to be parametrized as before, where the set of frequencies to be included is defined in the same way as for the red spin noise. Unlike when modelling the red spin noise, we no longer have the quadratic in the timing model to act as a proxy to the low-frequency ($\nu_s < 1/T$) DM variations in our data. As such these terms must be accounted for either by explicitly including these low frequencies in the model, or by including a quadratic in DM to act as a proxy, as with the red noise, defined as

$$Q_{\text{DM}}(t_i) = \alpha_0 t_i D_i + \alpha_1 t_i^2 D_i \quad (27)$$

with $\alpha_{0,1}$ free parameters to be fit for, and t_i the barycentric arrival time for TOA i . This can be achieved most simply by adding the timing model parameters DM1 and DM2 into the pulsar parameter file, and allowing TEMPONEST to include them in the fit.

3.3.2 Time domain power-law model

For a detailed discussion of this approach, and comparisons to existing methods see Lee et al. (2013). In brief, we transform our red noise covariance matrix $\mathbf{C}_{ij}^{\text{Red}}$ to

$$C_{ij}^{\text{DM}} = C_{ij}^{\text{Red}} D_i D_j. \quad (28)$$

The total noise covariance matrix can therefore be rewritten as

$$\mathbf{C}^{\text{tot}} = \mathbf{C}^{\text{Red}} + \mathbf{N} + \mathbf{C}^{\text{DM}}. \quad (29)$$

4 ANALYTICAL MARGINALIZATION OVER THE TIMING MODEL

Despite having the ability to fit simultaneously for all the timing model parameters and the stochastic properties of the noise present in the signal, there may be times where it is preferable to marginalize over some of the timing model parameters analytically in order to decrease the dimensionality of the problem. For example, a set of TOAs for a single pulsar might be the combination of many different sets of observations taken by different observatories, with phase jumps fitted between each set. If the specific values of these jumps are not of interest then the analysis might be performed faster if the decrease in the number of calculations required to explore the smaller dimensional space outweighs the increase in the calculation time that results from the matrix operations required by the marginalization process.

If we separate the timing model into a contribution from the set of parameters that we wish to parametrize $\boldsymbol{\tau}(\boldsymbol{\epsilon})$ and a contribution from the set of m parameters that we plan to marginalize over analytically $\boldsymbol{\tau}(\boldsymbol{\epsilon}')$, then we can write the probability that the data \mathbf{t} is described by the remaining parameters $\boldsymbol{\epsilon}$ and any additional parameters $\boldsymbol{\theta}$ we wish to include as

$$\Pr(\mathbf{t}|\boldsymbol{\epsilon}, \boldsymbol{\theta}) = \int d^m \boldsymbol{\epsilon}' \Pr(\boldsymbol{\epsilon}') \Pr(\mathbf{t}|\boldsymbol{\epsilon}', \boldsymbol{\epsilon}, \boldsymbol{\theta}). \quad (30)$$

Using a uniform prior on the m $\boldsymbol{\epsilon}'$ parameters, we use the same approach as described in vHL2013 to perform this marginalization

process analytically. This results in a set of equations (31) and (32) that exist in parallel to equations (17) and (21):

$$\Pr(t|\epsilon, \alpha, \beta) = \frac{1}{\sqrt{(2\pi)^{n-m} \det(\mathbf{G}^T \mathbf{C} \mathbf{G})}} \times \exp\left(-\frac{1}{2}(\delta t)^T \mathbf{G} (\mathbf{G}^T \mathbf{C} \mathbf{G})^{-1} \mathbf{G}^T (\delta t)\right), \quad (31)$$

where $\delta t = t - \tau(\epsilon)$, \mathbf{C} is the $n \times n$ noise covariance matrix as before and \mathbf{G} is the $n \times (n-m)$ matrix that performs the marginalization whose derivation will not be given here but is described in vHL2013,

$$\Pr(\epsilon, \alpha, \beta, \{\varphi_i\}|t) \propto \frac{\det(\hat{\Sigma})^{-1/2}}{\sqrt{\det(\varphi) \det(\hat{\mathbf{N}})}} \times \exp\left[-\frac{1}{2}\left(\delta t^T \hat{\mathbf{N}}^{-1} \delta t - \hat{\mathbf{d}}^T \hat{\Sigma}^{-1} \hat{\mathbf{d}}\right)\right], \quad (32)$$

where $\hat{\mathbf{N}} = \mathbf{G}(\mathbf{G}^T \mathbf{N} \mathbf{G})^{-1} \mathbf{G}^T$, $\hat{\Sigma} = (\mathbf{F}^T \hat{\mathbf{N}}^{-1} \mathbf{F} + \varphi^{-1})$ and $\hat{\mathbf{d}} = \mathbf{F}^T \hat{\mathbf{N}}^{-1} \delta t$.

5 LINEAR APPROXIMATION TO THE TIMING MODEL

We would like to compare the results of the non-linear analysis of the timing model afforded by TEMPONEST, with those that can be obtained from the linear approximation, and so we provide a brief description of the linear model below.

Given an initial estimate of the m timing model parameters ϵ_{0i} a linear approximation can be performed such that any deviations from that estimate are encapsulated using the m parameters $\delta\epsilon_i$ such that

$$\delta\epsilon_i = \epsilon_i - \epsilon_{0i}. \quad (33)$$

Therefore, writing the set of post-fit residuals that results from the subtraction of the initial estimate of the timing model from our TOAs as δt_{post} , we can express the change in these residuals that results from the deviation in the timing model parameters $\delta\epsilon$ as

$$\delta t = \delta t_{\text{post}} - \mathbf{M}\delta\epsilon, \quad (34)$$

where \mathbf{M} is the $n \times m$ ‘design matrix’ which describes the dependence of the timing residuals on the model parameters.

Therefore, in all previous equations, we can simply substitute $t - \tau(\epsilon)$ for $\delta t_{\text{post}} - \mathbf{M}\delta\epsilon$ in order to evaluate the linear approximation to the timing model.

6 APPLICATION TO SIMULATED DATA

In order to compare the parameter estimates obtained through both the non-linear and the linearized timing models, we use a series of three simulations, details of which are given below. The simulations are designed to make it progressively more difficult to extract the correct timing model parameters, due to both increasing the amplitude of the white noise in the data, and increasing the complexity of the noise by including additional red noise signals.

Simulation 1. The TOAs consist only of the deterministic timing model and Gaussian white noise with an amplitude of 10^{-7} s.

Simulation 2. As simulation 1, however with a white noise amplitude of 10^{-6} s.

Simulation 3. As simulation 1, however with the addition of a red noise signal described by equation (19) with $A = 5 \times 10^{-14}$ and $\gamma = 4.333$.

In all three simulations, we use a simulated timing model for the binary pulsar J1713+0747 consistent with current observed values (Splaver et al. 2005), details of which are given in Table 1. When performing the linearized parametrization of the timing model, we perform the linearization at the injected parameter values in order to maximize the performance of the method, and thus provide the most stringent comparison.

Tables 2–4 show the maximum likelihood, linear and non-linear timing model and stochastic parameter estimates for the three simulations. In all cases, we list only a single set of maximum likelihood parameter estimates, as these are the same for both linear and non-linear models. Figs 1–3 then show the one- and two-dimensional marginalized posteriors for a subset of the non-linear (top plots) and linear (bottom plots) timing model parameters related to the binary properties of the system that show the greatest differences when comparing the two models. For simulation 3, we substitute two of the timing model parameters in these plots (the orbital period and eccentricity) in favour of the spectral index and amplitude of the red noise.

For the three simulations, all the posterior distributions for the timing model parameters shown in Figs 1–3 are consistent with the injected parameter values within 2σ confidence intervals for both the linear and non-linear timing models. From simulation 1, we see that in the high signal-to-noise regime, there is almost no observable difference between either the parameter estimates or their uncertainties for the linear and non-linear timing models. This is to be expected as the range of parameter space over which the likelihood remains high is small, and thus the linear approximation should be valid.

As we increase the level of the white noise however, from an amplitude of 100 ns to 1 μ s, we begin to see some significant differences between the two models. In particular, the companion mass and Kopeikin parameters (KOM and KIN) show large curving degeneracies between the parameters. These non-Gaussian features are lost when we transition to the linear regime, which has the result of incorrectly estimating the uncertainties in these parameters. For example, the 1σ confidence intervals for the companion mass $M2$ is a factor 2.4 times smaller in the linear regime when compared to the non-linear.

This effect is accentuated even further in simulation three where we introduce a red noise signal into the data. Here, almost all parameters shown in Fig. 3 show an underestimation of the error in the linear regime, with the most extreme examples showing 1σ confidence intervals 8.8 and 10.8 times greater in the non-linear model for parameters $A1$ and $M2$, respectively. It is important to note that in both cases, we are modelling the red noise in the same way, and thus, this effect is solely due to the differences between the linear and non-linear timing models. As such, any method of pulsar timing analysis that operates in the linear regime, regardless of how it incorporates additional stochastic processes, such as the Cholesky method in C11, will suffer from this effect.

In this set of simulations, we do not see any significant bias in the timing model parameters returned by the linear timing model; however, given that the posterior probability distribution of the non-linear timing model shows significant curving degeneracies, and much greater 1σ confidence intervals for the binary parameters when compared to the linear model as the noise increases, we would expect that over a large number of realizations the number

Table 1. Injected timing model parameter values for PSR J1713+0747.

Fit and data set	
Pulsar name	J1713+0747
MJD range	500 00.3–530 02.0
Number of TOAs	216
Measured quantities	
Right ascension, α	17:13:49.532 5545
Declination, δ	+07:47:37.499 98
Pulse frequency, ν (s $^{-1}$)	218.811 840 441 434 861 31
First derivative of pulse frequency, $\dot{\nu}$ (s $^{-2}$)	-4.083 924 810 941 944 8511 $\times 10^{-16}$
Dispersion measure, DM (cm $^{-3}$ pc)	15.9936
Proper motion in right ascension, μ_α (mas yr $^{-1}$)	4.916 126 25
Proper motion in declination, μ_δ (mas yr $^{-1}$)	-3.920 8688
Parallax, π (mas)	0.935 9045
Orbital period, P_b (d)	67.825 129 6839
Epoch of periastron, T_0 (MJD)	543 03.635 387 74
Projected semimajor axis of orbit, x (lt-s)	32.342 422 339 04
Longitude of periastron, ω_0 (deg)	176.204 156 71
Orbital eccentricity, e	7.494 025 9711 $\times 10^{-5}$
First derivative of orbital period, \dot{P}_b	3.001 66 $\times 10^{-13}$
Periastron advance, $\dot{\omega}$ (deg yr $^{-1}$)	-3.6932 $\times 10^{-5}$
Companion mass, M_c (M $_{\odot}$)	0.311 2297
Longitude of ascending node, Ω (deg)	93.905 81
Orbital inclination angle, i (deg)	71.1391 53
Set quantities	
Epoch of frequency determination (MJD)	543 12
Epoch of position determination (MJD)	543 12
Epoch of DM determination (MJD)	543 12
Assumptions	
Clock correction procedure	TT(TAI)
Solar system ephemeris model	DE421
Binary model	T2
Model version number	5.00

Table 2. Maximum likelihood, non-linear and linear timing model parameter estimates for simulation 1.

	Maximum likelihood	Non-linear	Linear
Right ascension, α	4.510 914 902	4.510 914 902 (3)	4.510 914 902 (3)
Declination, δ	0.136 026 5985	0.136 026 5984 (3)	0.136 026 5984 (3)
Pulse frequency, ν (s $^{-1}$)	218.811 840 441 434 92	218.811 840 441 434 86 (18)	218.811 840 441 434 86 (18)
First derivative of pulse frequency, $\dot{\nu}$ (s $^{-2}$)	-4.083 922 $\times 10^{-16}$	-4.083 925 (6) $\times 10^{-16}$	-4.083 922 (6) $\times 10^{-16}$
Proper motion in right ascension, μ_α (mas yr $^{-1}$)	4.9186	4.9161 (18)	4.9161 (18)
Proper motion in declination, μ_δ (mas yr $^{-1}$)	-3.922	-3.921 (3)	-3.921 (3)
Parallax, π (mas)	0.94	0.94 (2)	0.94 (2)
Orbital period, P_b (d)	67.825 130	67.825 129 (7)	67.825 130 (7)
Epoch of periastron, T_0 (MJD)	543 03.6354	543 03.6354 (4)	543 03.6354 (4)
Projected semimajor axis of orbit, x (lt-s)	32.342 422 27	32.342 422 33 (16)	32.342 422 33 (16)
Longitude of periastron, ω_0 (deg)	176.204	176.204 (2)	176.204 (2)
Orbital eccentricity, e	7.494 10 $\times 10^{-5}$	7.494 02 (6) $\times 10^{-5}$	7.494 02 (6) $\times 10^{-5}$
First derivative of orbital period, \dot{P}_b	2×10^{-14}	$3 (6) \times 10^{-13}$	$3 (6) \times 10^{-13}$
Periastron advance, $\dot{\omega}$ (deg yr $^{-1}$)	-4×10^{-5}	$-3 (19) \times 10^{-5}$	$-3 (19) \times 10^{-5}$
Companion mass, M_c (M $_{\odot}$)	0.316	0.312 (16)	0.312 (16)
Longitude of ascending node, Ω (deg)	94.1	93.8 (1.4)	93.9 (1.4)
Orbital inclination angle, i (deg)	71.0	71.1 (6)	71.1 (7)

of occurrences of $>4\sigma$ deviations that occur in the linear timing model should exceed that predicted by Gaussian statistics. In order to test this hypothesis, we generate a series of 10 591 realizations of the noise in simulation 2, using TEMPO2 to calculate the parameter estimates with the linear timing model, and count the number of $>4\sigma_{T2}$ deviations for the binary parameters in the timing model,

with σ_{T2} the 1σ uncertainty returned by TEMPO2. Given Gaussian statistics, we would expect ~ 10 such events across all parameters total. Fig. 4 shows a histogram for the number of events for the binary parameters in PSR J1713+0747. The model parameters A1, M2, KIN and KOM show a significant excess from the Gaussian prediction, indicating that the linear timing model significantly

Table 3. Maximum likelihood, non-linear and linear timing model parameter estimates for simulation 2.

	Maximum likelihood	Non-linear	Linear
Right ascension, α	4.510 914 90	4.510 914 86 (3)	4.510 914 86 (2)
Declination, δ	0.136 026 598	0.136 026 602 (3)	0.136 026 602 (3)
Pulse frequency, ν (s $^{-1}$)	218.811 840 441 4366	218.811 840 441 4348 (18)	218.811 840 441 4348 (18)
First derivative of pulse frequency, $\dot{\nu}$ (s $^{-2}$)	$-4.083 85 \times 10^{-16}$	$-4.083 92 (6) \times 10^{-16}$	$-4.083 92 (6) \times 10^{-16}$
Proper motion in right ascension, μ_α (mas yr $^{-1}$)	4.906	4.905 (17)	4.906 (17)
Proper motion in declination, μ_δ (mas yr $^{-1}$)	-3.90	-3.91 (3)	-3.91 (3)
Parallax, π (mas)	1.2	1.0 (2)	0.9 (2)
Orbital period, P_b (d)	67.825 13	67.825 10 (6)	67.825 10 (6)
Epoch of periastron, T_0 (MJD)	543 03.635	543 03.636 (4)	543 03.634 (4)
Projected semimajor axis of orbit, x (lt-s)	32.342 422	32.342 421 (22)	32.342 422 (16)
Longitude of periastron, ω_0 (deg)	176.20	176.21 (2)	176.20 (2)
Orbital eccentricity, e	7.4948×10^{-5}	$7.4948 (6) \times 10^{-5}$	$7.4949 (6) \times 10^{-5}$
First derivative of orbital period, \dot{P}_b	-1.7×10^{-12}	$1.5 (65) \times 10^{-13}$	$5 (62) \times 10^{-13}$
Periastron advance, $\dot{\omega}$ (deg yr $^{-1}$)	-4×10^{-5}	$-9 (18) \times 10^{-4}$	$-10 (19) \times 10^{-4}$
Companion mass, M_c (M $_{\odot}$)	0.3	0.53 (27)	0.34 (13)
Longitude of ascending node, Ω (deg)	95	103 (13)	102 (16)
Orbital inclination angle, i (deg)	69	63 (8)	68 (6)

Table 4. Maximum likelihood, non-linear and linear timing model parameter estimates for simulation 3.

	Maximum likelihood	Non-linear	Linear
Right ascension, α	4.510 914 91	4.510 914 87 (2)	4.510 914 907 (9)
Declination, δ	0.136 026 597	0.136 026 601 (3)	0.136 026 5978 (18)
Pulse frequency, ν (s $^{-1}$)	218.811 840 4414	218.811 840 4412 (2)	218.811 840 4412 (2)
First derivative of pulse frequency, $\dot{\nu}$ (s $^{-2}$)	-4.084×10^{-16}	$-4.091 (4) \times 10^{-16}$	$-4.090 (4) \times 10^{-16}$
Proper motion in right ascension, μ_α (mas yr $^{-1}$)	4.93	4.94(2)	4.93 (2)
Proper motion in declination, μ_δ (mas yr $^{-1}$)	-3.94	-3.93 (4)	-3.93 (4)
Parallax, π (mas)	0.5	0.6 (2)	0.4 (2)
Orbital period, P_b (d)	67.825 13	67.825 16 (7)	67.825 15 (7)
Epoch of periastron, T_0 (MJD)	543 03.635	543 03.649 (11)	543 03.639 (4)
Projected semimajor axis of orbit, x (lt-s)	32.342 422	32.342 412 (12)	32.342 4211 (12)
Longitude of periastron, ω_0 (deg)	176.20	176.28 (6)	176.22 (2)
Orbital eccentricity, e	7.4938×10^{-5}	$7.4932 (8) \times 10^{-5}$	$7.4936 (6) \times 10^{-5}$
First derivative of orbital period, \dot{P}_b	4×10^{-12}	$7 (6) \times 10^{-12}$	$6 (6) \times 10^{-12}$
Periastron advance, $\dot{\omega}$ (deg yr $^{-1}$)	0.0016	0.0007 (18)	0.0007 (19)
Companion mass, M_c (M $_{\odot}$)	0.3	2 (3)	0.44 (13)
Longitude of ascending node, Ω (deg)	91	108 (13)	98 (18)
Orbital inclination angle, i (deg)	72	52 (13)	66 (7)
$\log_{10} A_{\text{red}}$	-13.01	-13.31 (19)	-13.31 (20)
Spectral index	3.5	4.7(7)	4.7 (7)

underestimates the errors in these parameters. Comparing this result to Fig. 2, we see that these parameters correspond to those that have large curving degeneracies in the posterior probability distribution, with significantly larger 1σ confidence intervals than those returned by the linear model, confirming our hypothesis.

7 APPLICATION TO REAL DATA

We now demonstrate the application of TEMPONEST to the publicly available data sets for the binary pulsar B1855+09 and the isolated pulsar B1937+21 presented in Kaspi, Taylor & Ryba (1994, henceforth K94). For the former, we demonstrate the ability of TEMPONEST to perform rigorous model selection between different sets of stochastic and timing model parameters, whilst for the latter, we compare power-law and model-independent descriptions of the red spin noise, and in addition to these, also compare the method of Keith et al. (2013) in our analysis of the DM variations in order to find the optimal description of the stochastic properties of the data.

7.1 B1855+09

The mean posterior values and associated 1σ errors for the final fitted timing model and stochastic parameters for PSR B1855+09 are listed in Table 5 and includes five astrometric quantities ($\alpha, \delta, \mu_\alpha, \mu_\delta, \pi$), two rotational parameters ($\nu, \dot{\nu}$), DM, as well as seven binary parameters. In addition to these, we have included three stochastic parameters, an EFAC, EQUAD and a single red noise power spectrum coefficient, with a frequency equal to $1/T$, with T the total time span of the data.

In performing the analysis using TEMPONEST, we first performed a series of 10 iterations with TEMPO2 to ensure that the timing solution had converged and to set a uniform prior on the timing model parameters covering a range of $\pm 10\sigma_{T_2}$ from the maximum likelihood estimate obtained from the final iteration with σ_{T_2} the error returned by TEMPO2. The maximum likelihood TEMPO2 estimates and 1σ errors are given in Table 5 alongside the TEMPONEST results. For the stochastic parameters, we took our priors to be uniform across the ranges [0, 5], [-10, -5], [-20, 0] for EFAC, \log_{10} EQUAD and ρ_i , respectively.



Figure 1. One- and two-dimensional marginalized posterior distributions for a subset of the binary parameters for PSR J1713+0747 for simulation 1 for the non-linear (top) and linear (bottom) timing models. These parameters are from left to right: the orbital period of the binary (PB), the epoch of periastron (T0), the projected semimajor axis of orbit (A1), the longitude of periastron (OM), the eccentricity (ECC), the first derivative of the orbital period of the binary (PBDOT), the first derivative of the longitude of periastron (OMDOT), the companion mass (M2), the longitude of ascending node (KOM) and the inclination angle (KIN). In all cases, the scale on the x -axis is the deviation from the injected parameter values in units of the uncertainty in the parameter returned by TEMPO2. In the high signal-to-noise regime of these simulations the two models are completely consistent with one another, both in terms of parameter estimates and uncertainties.

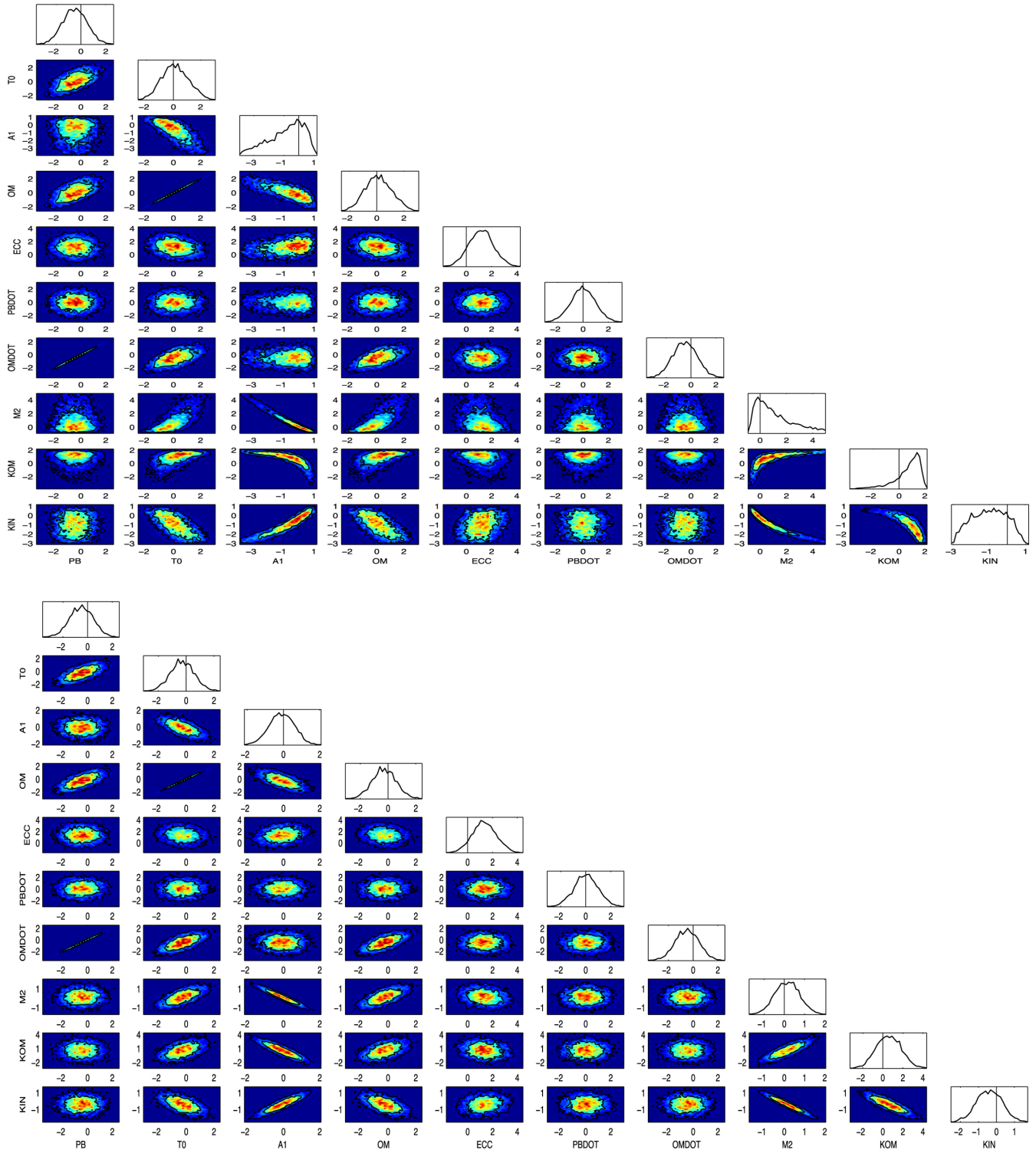


Figure 2. One- and two-dimensional marginalized posterior distributions for a subset of the binary parameters for PSR J1713+0747 for simulation 2 for the non-linear (top) and linear (bottom) timing models. These parameters are from left to right: the orbital period of the binary (PB), the epoch of periastron (T0), the projected semimajor axis of orbit (A1), the longitude of periastron (OM), the eccentricity (ECC), the first derivative of the orbital period of the binary (PBDOT), the first derivative of the longitude of periastron (OMDOT), the companion mass (M2), the longitude of ascending node (KOM) and the inclination angle (KIN). In all cases, the scale on the x -axis is the deviation from the injected parameter values in units of the uncertainty in the parameter returned by TEMPO2. With the increase in the level of the white noise ($1\ \mu\text{s}$), there are now significant differences in the posterior distributions of the two timing models with large non-Gaussian tails leading to an underestimation of the uncertainties in the linear model.

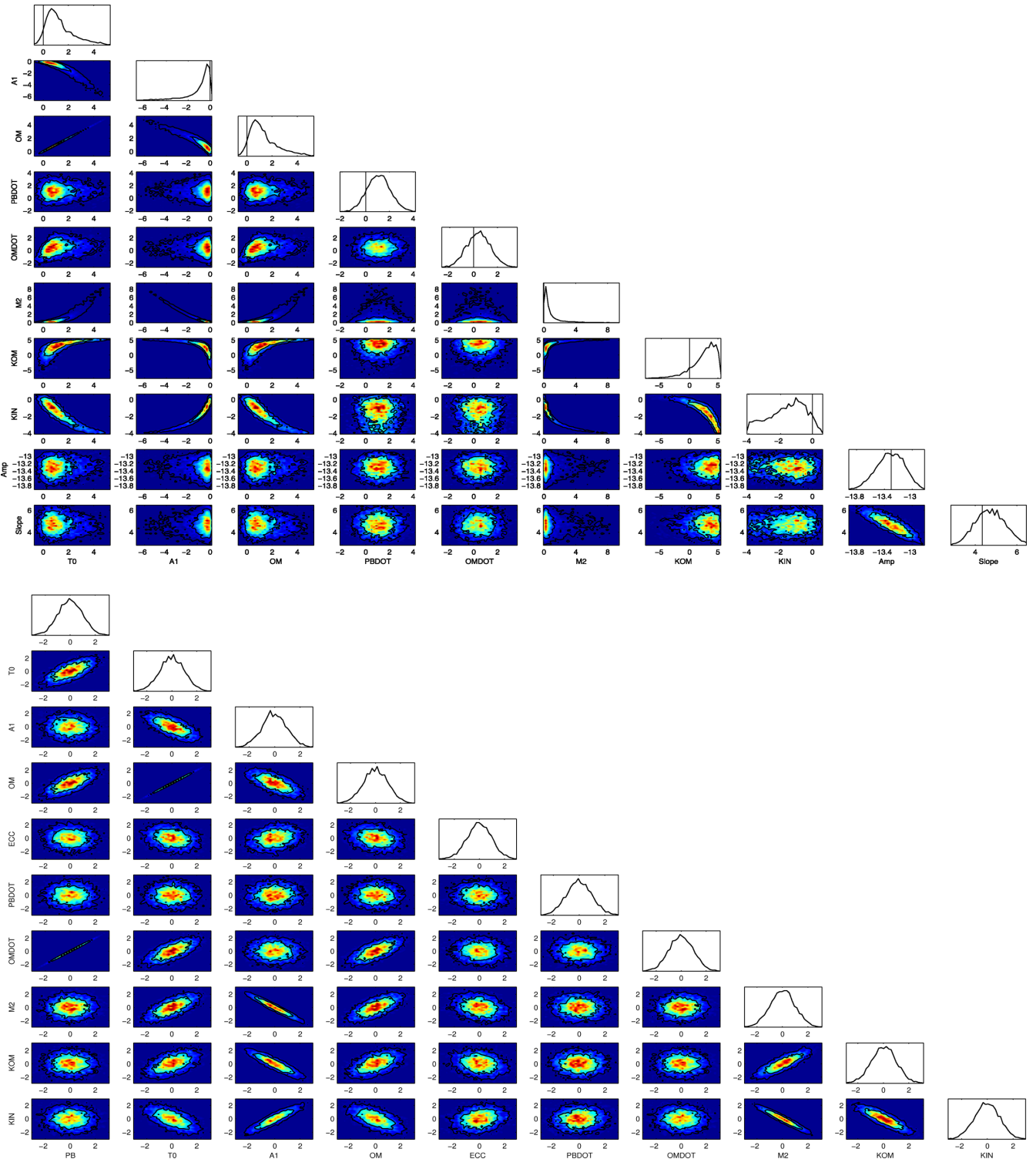


Figure 3. One- and two-dimensional marginalized posterior distributions for a subset of the binary parameters for PSR J1713+0747 for simulation 3 for the non-linear (top) and linear (bottom) timing models. These parameters are from left to right: the epoch of periastron (T_0), the projected semimajor axis of orbit (A_1), the longitude of periastron (OM), the first derivative of the orbital period of the binary ($PBDOT$), the first derivative of the longitude of periastron ($OMDOT$), the companion mass (M_2), the longitude of ascending node (KOM) and the inclination angle (KIN). In all cases, but the red noise parameters, the scale on the x -axis is the deviation from the injected parameter values in units of the uncertainty in the parameter returned by TEMPO2. Whilst all parameters are consistent with the injected values within 2σ confidence intervals, the addition of red noise to the signal has resulted in even greater discrepancies in the estimated parameter uncertainties between the linear and non-linear timing models; however, the posterior distributions for the two stochastic parameters are extremely consistent between both.

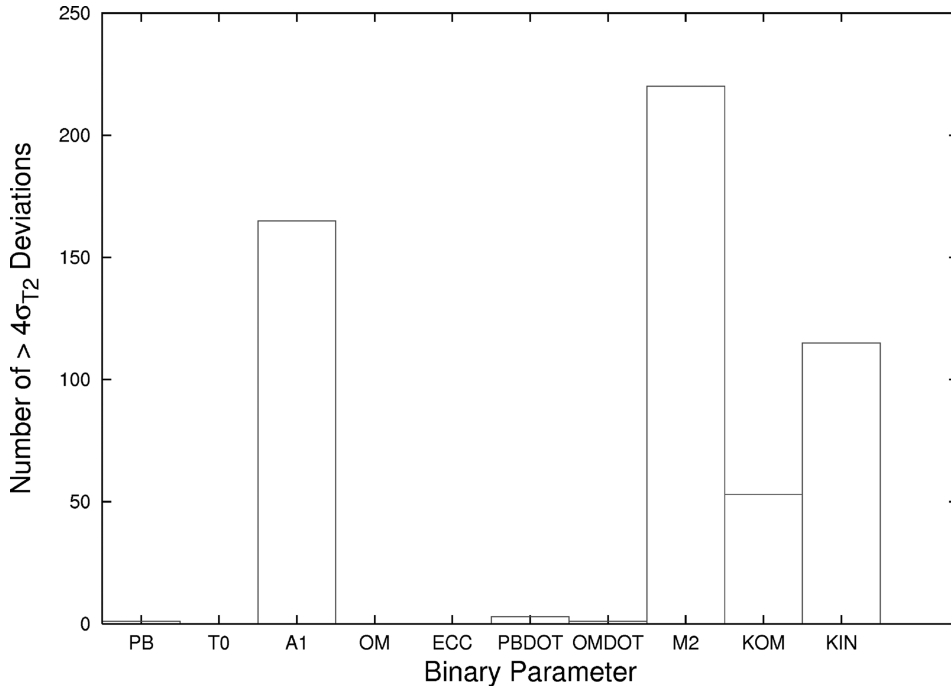


Figure 4. Number of greater than $4\sigma_{T_2}$ deviations for the binary parameters in the timing model of PSR J1713+0747 between the fit returned by TEMPO2 using the linear timing model and the true value in a series of 10 591 realizations of the noise in simulation 2, with σ_{T_2} the 1σ uncertainty returned by TEMPO2. Given Gaussian statistics, we would expect ~ 10 such events across all parameters total. The model parameters A1, M2, KIN and KOM show significant deviations from this prediction, indicating that the linear timing model significantly underestimates the errors in these parameters. Comparing this result to Fig. 2, we see that these parameters correspond to those that have large curving degeneracies in the posterior probability distribution, with significantly larger 1σ confidence intervals than those returned by the linear model.

In addition to these quantities, Table 5 lists the parameter estimates for four additional timing model parameters, $\dot{\omega}$, \dot{P}_b , \dot{e} and \dot{x} which were added to the timing model one at a time and the full analysis repeated. In all cases, however, the addition of the extra timing model parameters resulted in a decrease of the log-evidence by ~ 1 unit relative to the original fit indicating that there is no support for the parameters in the data.

Comparing the evidence for a model without the three stochastic parameters to that in Table 5, we find a decrease of the log-evidence of ~ 2.5 units. Whilst this is not definitive, the inclusion of the stochastic parameters is still strongly favoured, and allows us to quantify the qualitative observation of a cubic signal present in the residuals described in Kaspi (1995).

Finally, because the observations of B1855+09 presented in K94 were made using three observing back-ends over the course of the data set, we also performed the analysis including two jumps between the different systems. As there is a strong covariance between red noise signals and the jump parameters, we included the following combinations of parameters in our analysis:

- (i) Model 1: Including jumps – without any additional stochastic parameters.
- (ii) Model 2: Including jumps – including EFAC/EQUAD.
- (iii) Model 3: Including jumps – including EFAC/EQUAD and a single red noise coefficient at frequency $1/T$.

As with the other timing model parameters, we set our prior to be $\pm 10\sigma_{T_2}$ from the TEMPO2 initial estimate. We could then compare the evidence returned from these analyses, with those models that exclude the jump parameters to see which set is most supported by the data. In every instance the inclusion of the jumps resulted in either a small drop in the evidence of ~ 0.5 , or it remained the

same, suggesting no support for these parameters in the data. The parameter estimates for the jumps when fitted alongside the optimal set of parameters are listed in Table 5 alongside the other additional parameters tested.

Comparing the parameter estimates obtained by TEMPONEST with those from TEMPO2, we see that they are completely consistent for all values and their uncertainties. Such agreement is unsurprising as the approximation that the data are well described by only the timing model and white noise is well justified in this instance given the minor support for additional stochastic parameters in the data.

7.2 B1937+21

In comparison to B1855+09, the timing model for pulsar B1937+21 is relatively simple, requiring only eight parameters, the same five astrometric and two rotational quantities as for B1855+09, and DM. However, the analysis is made more complex by the presence of significant long-term variation in the timing residuals. In order to account for one source of this noise, the TOAs in the K94 data set were observed at two widely spaced frequencies, 1408 and 2380 MHz in order to calculate the effects of dispersion on the residuals prior to fitting the timing model.

In performing the analysis with TEMPONEST, we therefore use two versions of the TOAs. The first includes the DM corrections calculated in K94 (henceforth data set 1), and the second excludes them (henceforth data set 2). The simple timing model required for this pulsar means that we expect little non-linearity despite the large amounts of noise present in the data. We therefore first analytically marginalize over the timing model using the timing model estimates obtained from TEMPO2 and perform model selection between different sets of stochastic parameters for each data set. In each case,

Table 5. Timing model and stochastic parameter estimates for PSR B1855+09.

	Fit and data set	
Pulsar name	B1855+09	
MJD range	464 36.7–489 73.7	
Number of TOAs	270	
Evidence	3450.2 ± 0.3	
	Measured quantities	
	TEMPONEST	TEMPO2
Right ascension, α	18:57:36.394 354(4)	18:57:36.394 354(4)
Declination, δ	+09:43:17.319 66(10)	+09:43:17.319 66(11)
Pulse frequency, v (s^{-1})	186.494 407 877 865 23(4)	186.494 407 877 865 23(4)
First derivative of pulse frequency, \dot{v} (s^{-2})	-6.204 99(9) × 10 ⁻¹⁶	-6.205 00(9) × 10 ⁻¹⁶
Dispersion measure, DM (cm ⁻³ pc)	13.307(3)	13.308(3)
Proper motion in right ascension, μ_α (mas yr ⁻¹)	-2.63(3)	-2.63(3)
Proper motion in declination, μ_δ (mas yr ⁻¹)	-5.41(5)	-5.46(5)
Parallax, π (mas)	1.2(2)	1.1(3)
Sine of inclination angle, sin i	0.9991(4)	0.9990(4)
Orbital period, P_b (d)	12.327 171 3813(4)	12.327 171 3815(5)
Epoch of periastron, T_0 (MJD)	475 29.896(2)	475 29.8966(19)
Projected semimajor axis of orbit, x (lt-s)	9.230 7801(3)	9.230 7802(3)
Longitude of periastron, ω_0 (deg)	276.39(6)	276.39(6)
Orbital eccentricity, e	2.170(3) × 10 ⁻⁵	2.169(4) × 10 ⁻⁵
Companion mass, M_c (M _⊕)	0.270(14)	0.265(14)
	Stochastic parameters	
EFAC	0.806(11)	-
$\log_{10}[\text{EQUAD (s)}]$	-6.2(2)	-
$\log_{10} [\text{RedC1}]$	-4.5(1.0)	-
	Set quantities	
Epoch of frequency determination (MJD)	475 26	
Epoch of position determination (MJD)	475 26	
Epoch of DM determination (MJD)	475 26	
	Assumptions	
Clock correction procedure	TT(TAI)	
Solar system ephemeris model	DE405	
Binary model	T2	
Model version number	5.00	
	Additional included parameters	
First derivative of orbital eccentricity, \dot{e}	-2(5) × 10 ⁻¹⁶	
First derivative of orbital period, \dot{P}_b	0.2 (1.1) × 10 ⁻¹²	
First derivative of x , \dot{x}	1.5 (2.1) × 10 ⁻¹⁵	
Periastron advance, $\dot{\omega}$ (deg yr ⁻¹)	-0.01(4)	
Jump 1 mk3_14w	-1.8 (1.1) × 10 ⁻⁶	
Jump 2 mk3_14m	0.5 (1.9) × 10 ⁻⁷	

we include an EFAC and EQUAD parameter, and then test different combinations of models for the red noise and DM variations in the data. The full set of models compared in both data sets 1 and 2 are listed below.

(i) Data set 1

Model 1: model-independent analysis with N_c consecutive frequency coefficients.

Model 2: model-independent analysis with optimally chosen frequency coefficients.

Model 3: power-law analysis with N_c consecutive coefficients.

(ii) Data set 2

Model 1: model-independent analysis with N_c coefficients for both red noise and DM variations.

Model 2: power-law analysis with N_c coefficients for red noise, model-independent analysis of DM variations.

Model 3: model-independent analysis with N_c coefficients for red noise, power-law analysis for DM variations.

Model 4: power-law analysis with N_c coefficients for both red noise and DM variations.

7.2.1 Dataset 1

Table 6 shows the evidence returned for the different stochastic models applied to data set 1. Using the model-independent description of the red noise signal, we find that only six power spectrum coefficients are supported by the data when including consecutive frequencies. Whilst this may seem like a small number for an apparently complex signal, in L13 it is shown that even in the high signal-to-noise regime, over an order of magnitude fewer power

Table 6. Evidence for different stochastic models for pulsar B1937+21 in data set 1.

Model	N_c	log evidence
Model-independent analysis	5	0
-	6	2.8
-	7	2.7
-	8	2.7
-	10	2.3
-	15	-2.1
-	20	-6.5
Model-independent analysis with optimal frequencies	7	5.9
Power law	6	5.2
-	10	6.5
-	20	7.2
-	50	7.4
-	100	7.5
Two-component power law	100	8.7

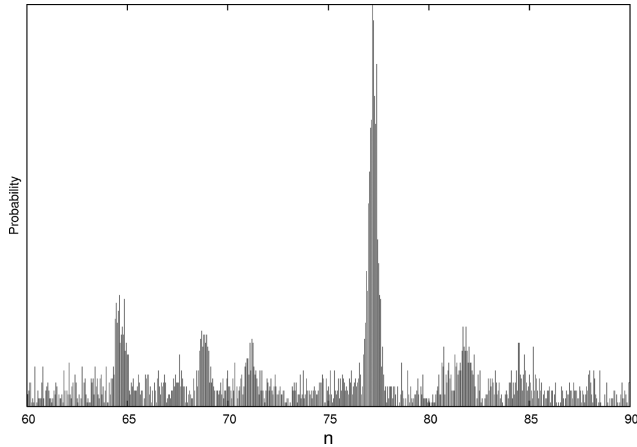


Figure 5. Subset of the posterior probability distribution for the frequency of the floating power spectrum coefficient in terms of n such that the frequency is given by $v = n/T$. Whilst several peaks are visible, only the inclusion of the dominant peak at $n = 77.2$ results in an increase of the evidence.

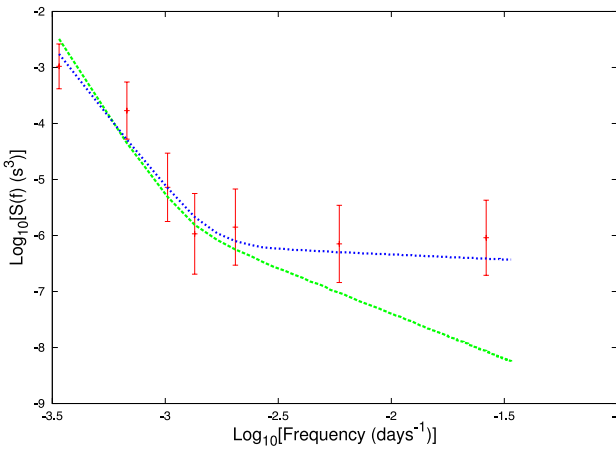


Figure 6. Left: the mean values and associated one sigma error bars for the power at the seven optimal frequencies fitted to B1937+21 data set 1 using the model-independent analysis. The blue dotted and green dashed lines indicate the mean two component power-law models fitted over the optimal set of frequencies only and over the first 100 consecutive frequencies, respectively. Whilst the two-component model fitted to only the optimal set is consistent at all frequencies, we include this only for completion as we do not consider it to be a physically motivated model. Right: timing residuals for B1937+21 data set 1 (red points) and the best-fitting signal realization for the red noise using the optimal model-independent analysis (blue dotted line).

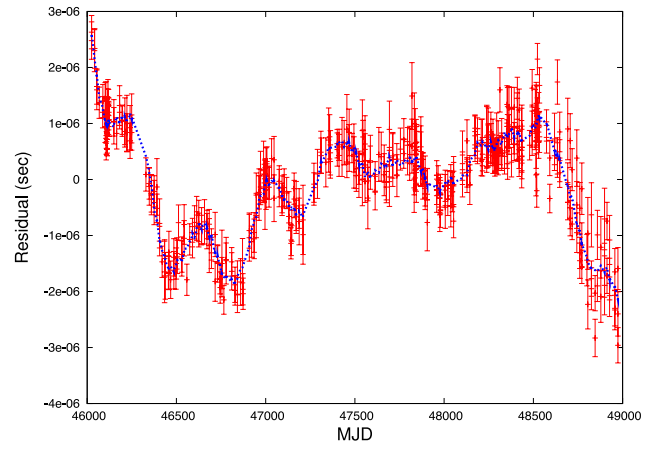
spectrum coefficients than time series data points are required to describe the data when dealing with steep red power spectrum.

It is possible, however, that frequencies with $n > 6$ are supported by the data but that considering only a consecutive set biases the model to include only low-frequency coefficients. To ascertain whether this is the case, we perform the following test:

- (1) include the lowest six power spectrum coefficients in the model red noise model;
- (2) in addition, include a coefficient with frequency a free parameter, allowed to vary continuously from $v = 6/T$ to $v = 100/T$;
- (3) include all frequencies at which there is a peak in the posterior probability distribution for this floating coefficient into the model;
- (4) eliminate coefficients until the optimal set is found, such that the evidence is maximized.

A different approach to follow could be that of Feroz, Balan & Hobson (2011). Here, the data would initially be analysed with one power spectrum coefficient, with frequency allowed to vary. In this stage, the evidence is not calculated, but the computationally less expensive process of parameter estimation is performed. The resulting best-fitting model is subtracted from the data and a set of residuals formed. An evidence calculation is then performed for two competing models on the residuals: (i) that the residuals contain a signal described by one power spectrum coefficient, or (ii) the data contain no signal. If the evidence supports the inclusion of an additional power spectrum coefficient the parameter estimation is repeated with two components and a new set of residuals formed. This process is then repeated until the evidence from the residual analysis no longer supports any signal. This has the advantage that the evidence calculation need only be performed for a single frequency, eliminating much of the computational cost; however, comparisons between this and other methods will be the subject of future work.

Fig. 5 shows a section of the posterior probability distribution for the frequency of the floating power spectrum coefficient. Whilst there are multiple modes in the posterior, only the inclusion of the dominant peak at a frequency of $n = 77.2/T$ is supported by the evidence. In total, the optimal set of frequencies was given by [1, 2, 3, 4, 6, 17.2, 77.2]. Using this optimal set increases the log evidence by ~ 3 over the model with six consecutive frequencies. Fig. 6 (left)



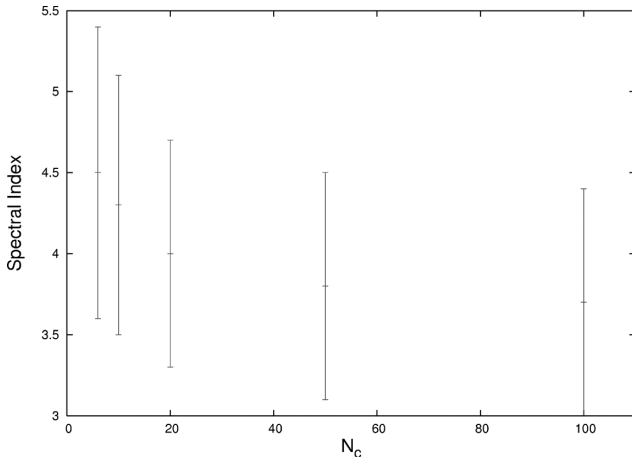


Figure 7. Mean spectral index and 1σ uncertainties for the power-law model fitted to B1937+21 data set 1. Whilst the uncertainties are large, there is a clear trend for the mean parameter estimate to move towards shallower spectral indices as the number of coefficients over which the model fit increases, and it intercepts the flat tail of the red spin noise spectrum.

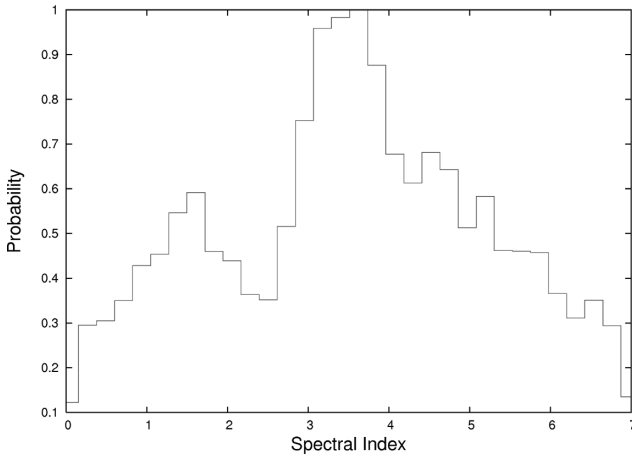


Figure 8. One-dimensional marginalized posterior for the spectral indices of the two component power-law model. Two peaks are clearly visible in the posterior, corresponding to a steep red noise process at low frequencies, and a shallower one at higher frequencies.

shows the power spectrum for the red spin noise evaluated at the optimal set of frequencies, whilst the right-hand panel shows the maximum likelihood signal realization given the mean parameter estimates for this optimal set. The power spectrum shows the clear signature of a steep red noise process at low frequencies, with a substantial, flatter, high-frequency tail.

When fitting a power-law model to the data, we find that the evidence stabilizes after $N_c \sim 20$. Despite the flat tail to the power

spectrum visible with the model-independent analysis, we observe an increase in the evidence of ~ 1 compared to the optimal frequency model. Fig. 7 shows the mean posterior value and 1σ uncertainties for the spectral indices of the power-law model fitted as we increase the number of coefficients included in the model. Whilst the uncertainties are large, the mean value shows a clear trend towards flatter values decreasing from 4.5 to 3.7 as the number of coefficients included increases from 6 to 100 and more of the flat spectrum tail is included in the model.

Given these results, we therefore also model the red noise as a two component power law. Fig. 8 shows the one-dimensional marginalized posterior for one of the spectral indices included in this model, displaying two clear peaks: one associated with the steep low-frequency part of the spectrum with an index of ~ 4 , and one with the flat spectrum tail with an index of ~ 1.5 . The evidence for the two-component fit results in a final increase of ~ 1 relative to the one-component model; however, we must subtract $\log 2$ from this value in order to account for ‘counting degeneracy’, the fact that we have two combinations of spectral indices (i.e. the parameters for the first and second power law can switch without affecting the result). Therefore, whilst there are tentative signs of this dual spectrum signal in the data, it is not sufficient to justify the additional parameters in our description of the stochastic signal; we therefore consider the one-component power law to be the optimal choice for this data set.

7.2.2 Data set 2

Table 7 lists the evidence for the different models applied to data set 2, where we give the value only for the optimal N_c in each case. In all cases, the number of coefficients required by the DM variations was greater than for the red noise. For data set 2, the optimal set of frequencies is given by [1, 2, 5, 6] for the red spin noise and [1, 2, 3, 4, 6, 8, 10, 11, 12, 13, 24.6, 81.5] for the DM variations. We find that once again finding the optimal set of frequencies to include results in a significant increase in the log evidence of ~ 4.5 when compared to the consecutive set. As with data set 1, we show in Fig. 9 the residuals and maximum likelihood signal realization given the mean posterior values for the power spectrum coefficients obtained by the optimal model-independent analysis. Fitting for a power-law model in both cases results in spectral indices of -5 ± 1 and -2.6 ± 0.4 for the red noise and DM variations, respectively, consistent with the model-independent analysis. As with data set 1, this consistency is supported by the log evidence, which has a maximum when constraining the power spectrum to follow a power law.

Compared to data set 1, we find that neither the red noise nor the DM variation power spectrum in data set 2 show any sign of a shallow tail. This suggests that the DM model applied in K94 did not account fully for the higher frequency DM variation, flattening the red noise spectrum of the resultant residuals.

Table 7. Evidence for different stochastic models for pulsar B1937+21 in data set 2.

Model	N_c (Red, DM)	log evidence
Model-independent red noise and DM with consecutive frequencies	2, 13	0
Model-independent red noise and DM with optimal frequencies	5, 12	4.3
Power-law red noise, model-independent DM with consecutive frequencies	10, 13	0.7
Model-independent red noise with consecutive frequencies, power-law DM	2, 15	11.5
Power-law red noise and DM	10, 15	11.9
Power-law red noise and two-component power-law DM	10, 100	11.5

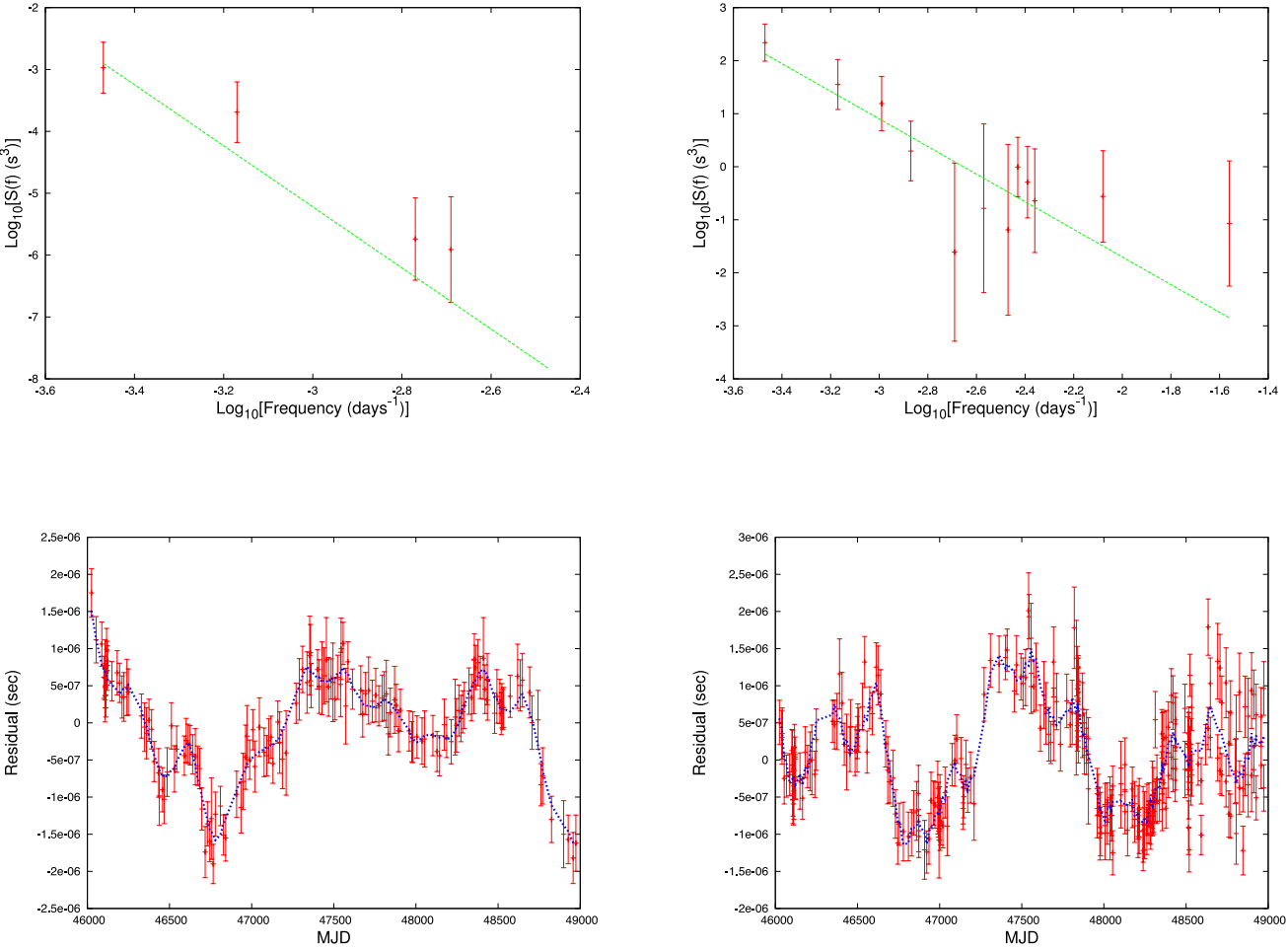


Figure 9. Top: mean values and 1σ uncertainties for the optimal set of power spectrum coefficients required to describe the red noise (left) and DM variations (right). The mean power-law estimate is over plotted in both cases, for which we find spectral indices of -5 ± 1 and -2.6 ± 0.4 calculated including the first 10 and 15 consecutive coefficients for each, respectively. Bottom: timing residuals for B1937+21 data set 2 (red points) and the best-fitting combined signal realization for the red noise and DM variations using the optimal model-independent analysis (blue dotted line) shown for the 2.4 GHz (left) and 1.4 GHz (right) data separately for clarity.

We now perform the analysis of the non-linear timing model simultaneously with the red noise and DM variations, where we model the latter two elements using a power-law model as has been supported by the evidence in the preceding stochastic analysis.

7.2.3 Timing model analysis

Table 8 lists the mean posterior values and associated 1σ uncertainties for our final timing model and stochastic solutions to both data sets 1 and 2 where, following the results in Sections 7.2.1 and 7.2.2, the stochastic signals have been modelled as power-law processes for both the red noise and DM variations. Fig. 10 then shows the one- and two-dimensional marginalized posteriors for a selection of the modelled parameters; RA, DEC, PMRA, PMDEC, PX and the red noise, and DM spectral indices and amplitudes. As expected, the timing model parameters show no evidence for non-linear behaviour in either case despite the high levels of red noise in the data set. As such, we would expect that our estimates for the stochastic parameters when analytically marginalizing over the timing model will be completely consistent with those in the full analysis, and indeed, this is the case in both data sets.

Table 8 also lists the timing model solutions returned by applying both the standard TEMPO2 fit and using the SpectralModel plug-in

which utilizes the Cholesky method described in C11. In order to use the SpectralModel plug-in in the case of data set 2, we therefore applied the method of Keith et al. (2013) to model the DM variations as a linearly interpolated time series, sampled every 100 d in the observation. Unlike the approach in K94, this therefore allows us to include the uncertainties in the DM model in the final timing model solutions whilst still using the Cholesky method.

Fig. 11 shows a graphical representation of the differences between the TEMPONEST, SpectralModel and TEMPO2 results for the timing model parameters given in Table 8 for data sets 1 (left) and 2 (right). Here, the value on the y-axis is given by the difference between the TEMPONEST (or SpectralModel) estimate and the TEMPO2 estimated parameter values, divided by the TEMPO2 error, which as before we will denote σ_{T2} . The errors are then the 1σ errors estimated by TEMPONEST (SpectralModel) which we will denote σ_{TN} (σ_{SM}). Therefore, a fit that is consistent both with the value and error returned by TEMPO2 would have a value of 0 ± 1 in Fig. 11.

There are several things that are immediately apparent in Fig. 11. The first is the level of disparity between the parameter estimates returned by TEMPO2, and those returned by both TEMPONEST and the SpectralModel analysis. With the exception of only DM in data set 1, and PX in data set 2, the parameter estimates returned by

Table 8. Timing model and stochastic parameter estimates for PSR B1937+21.

Fit and data set			
Pulsar name	B1937+21		
MJD range	460 24.8–489 73.8		
Number of TOAs	420		
Measured quantities – including K94 DM corrections			
	TEMPOEST	TEMPO2	SpectralModel
Right ascension, α	19:39:38.561 314(10)	19:39:38.561 288(3)	19:39:38.561 30(5)
Declination, δ	+21:34:59.1295(2)	+21:34:59.130 68(5)	+21:34:59.1291(9)
Pulse frequency, ν (s $^{-1}$)	641.928 233 558 03(16)	641.928 233 557 9857(7)	641.928 233 5581(14)
First derivative of pulse frequency, $\dot{\nu}$ (s $^{-2}$)	$-4.331\ 69(3) \times 10^{-14}$	$-4.331\ 6913(15) \times 10^{-14}$	$-4.331\ 69(5) \times 10^{-14}$
Dispersion measure, DM (cm $^{-3}$ pc)	71.040 03(2)	71.039 981(15)	71.040 024(15)
Proper motion in right ascension, μ_α (mas yr $^{-1}$)	0.084(11)	0.054(4)	0.08 (7)
Proper motion in declination, μ_δ (mas yr $^{-1}$)	-0.421(15)	-0.319(4)	-0.43(2)
Parallax, π (mas)	0.24(9)	0.01(4)	0.20(15)
EFAC	0.88(14)	–	–
$\log_{10}[\text{EQUAD (s)}]$	-6.59(4)	–	–
$\log_{10} A_{\text{red}}$	-3.30(16)	–	–
γ_{red}	3.9(6)	–	–
Measured quantities – excluding K94 DM corrections			
	TEMPOEST	TEMPO2	SpectralModel
Right ascension, α	19:39:38.561 307(10)	19:39:38.561 219(3)	19:39:38.561 301(19)
Declination, δ	+21:34:59.1296(2)	+21:34:59.131 36(5)	+21:34:59.1292(4)
Pulse frequency, ν (s $^{-1}$)	641.928 233 5581(3)	641.928 233 558 0713(13)	641.928 233 5581(9)
First derivative of pulse frequency, $\dot{\nu}$ (s $^{-2}$)	$-4.331\ 69(6) \times 10^{-14}$	$-4.331\ 679(3) \times 10^{-14}$	$-4.3317(2) \times 10^{-14}$
Dispersion measure, DM (cm $^{-3}$ pc)	71.041(13)	71.040 715(15)	71.040 60(12)
Proper motion in right ascension, μ_α (mas yr $^{-1}$)	0.069(10)	-0.005(3)	0.08(2)
Proper motion in declination, μ_δ (mas yr $^{-1}$)	-0.411(15)	-0.279(4)	-0.44(5)
Parallax, π (mas)	0.25(10)	0.41(4)	0.19(13)
EFAC	1.29(19)	–	–
$\log_{10}[\text{EQUAD (s)}]$	-7.3(9)	–	–
$\log_{10} A_{\text{red}}$	-3.7(3)	–	–
γ_{red}	5.3(9)	–	–
$\log_{10} A_{\text{DM}}$	-0.15(7)	–	–
γ_{DM}	2.7(3)	–	–
Set quantities			
Epoch of frequency determination (MJD)	526 01		
Epoch of position determination (MJD)	526 01		
Epoch of DM determination (MJD)	526 01		
Assumptions			
Clock correction procedure	TT(TAI)		
Solar system ephemeris model	DE405		
Binary model	NONE		
Model version number	5.00		

TEMPOEST during the joint analysis are at least $4\sigma_{T_2}$ away from the TEMPO2 values, with an average deviation of $\sim 30\sigma_{T_2}$.

Whilst the parameter estimates returned by the TEMPOEST and SpectralModel analysis are in both cases consistent with one another, the estimates of the uncertainties are several times larger than those returned by TEMPOEST by a factor of $\sim 2\text{--}3$.

In order to investigate the difference in the uncertainties returned by TEMPOEST and the SpectralModel plug-in, we first consider the major differences between the different types of analysis.

(i) TEMPOEST uses the full non-linear model compared to the linear approximation in SpectralModel;

(ii) TEMPOEST uses physical priors on parameters such as parallax, such that they must take values greater than zero, SpectralModel does not;

(iii) TEMPOEST includes both red and white noise estimation in the fit with the timing model, SpectralModel does not include additional

white noise terms, and fixes the red noise when calculating the uncertainties for the timing model;

(iv) TEMPOEST uses a cut-off power-law model for the red noise, whereas SpectralModel uses a red noise model with a corner frequency at which it turns over.

In order to ascertain how large an effect these differences make, we therefore rerun the analysis on data set 1, so that we have the same DM model in both cases, whilst making the following changes:

(1) use the linear timing model, linearized at the timing model parameters estimated by the SpectralModel plug-in without the condition that parameters must take physical values;

(2) as in (1), but fixing EFAC = 1 and EQUAD = 0, and fixing the spectral index of the red noise power law to be the same value used in the SpectralModel plug-in (-4.0).

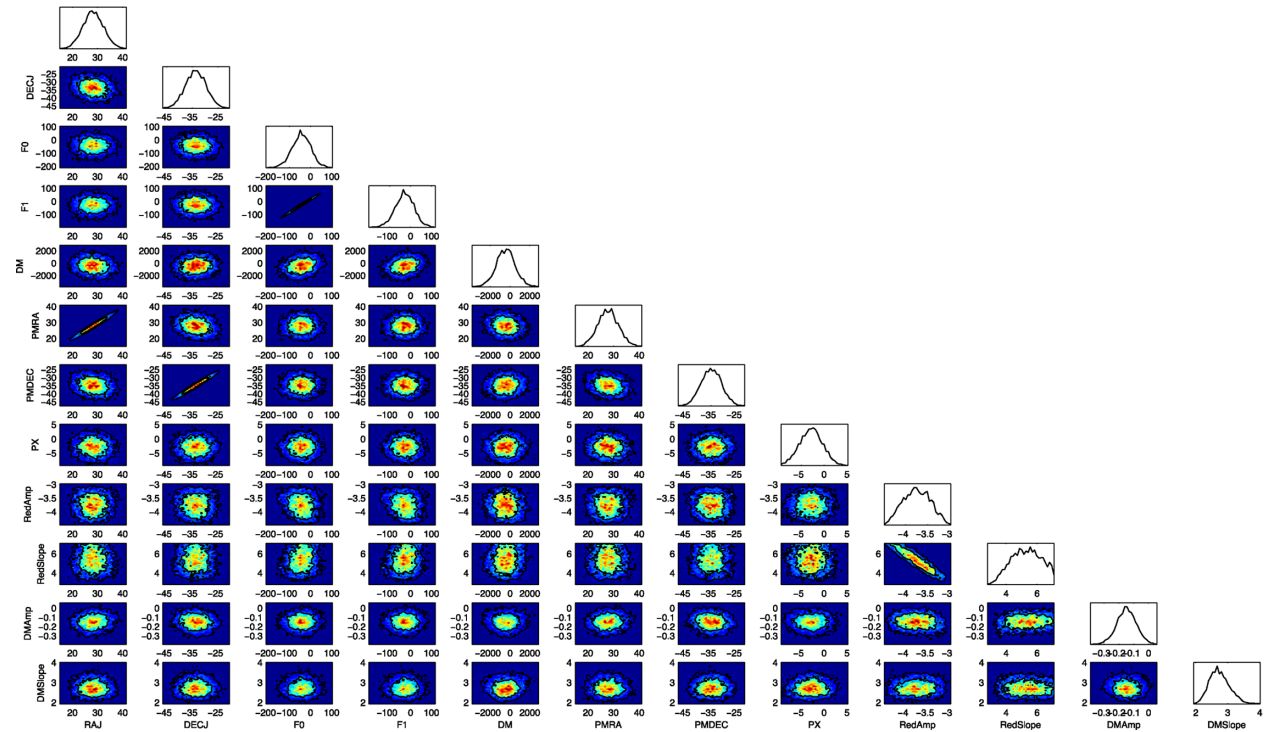
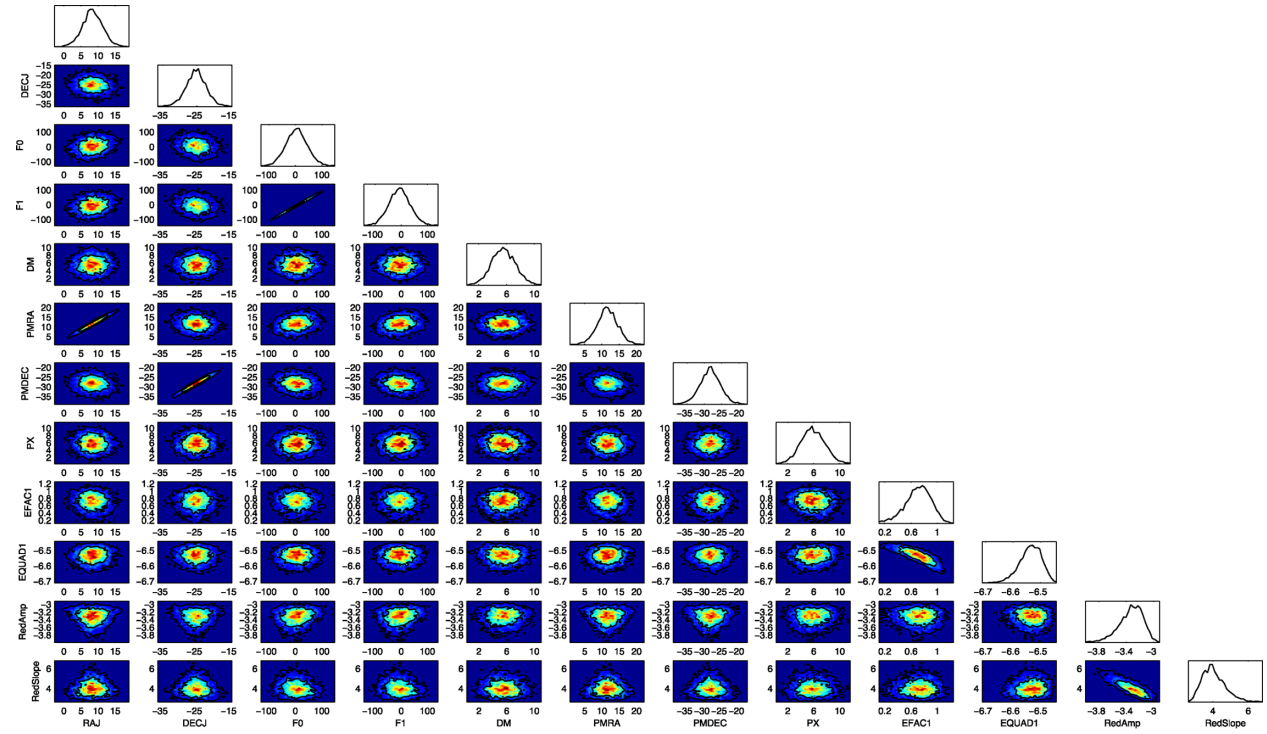


Figure 10. Top: the one- and two-dimensional marginalized posterior distributions for the eight timing model parameters: RA, DEC, F0, F1, DM, PMRA, PMDEC and PX, and the four stochastic parameters: EFAC, EQUAD, and amplitude and spectral index of the power-law model for the red noise for data set 1. Bottom: as in the top plot, but for data set 2, and with EFAC and EQUAD replaced with the amplitude and spectral index of the power-law model for DM variations.

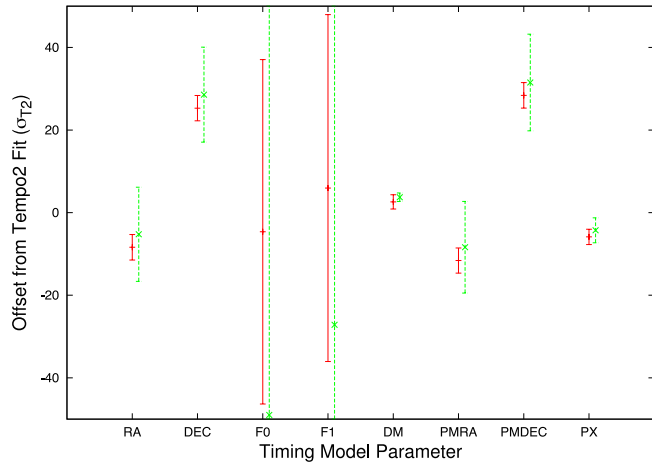


Figure 11. Left: difference between the parameter estimates and uncertainties returned by TEMPONEST (red solid points) and the SpectralModel plug-in (green points) and TEMPO2 for PSR B1937+21 for data set 1. Right: as with the left-hand plot, but for data set 2, where we have used DM model to characterize the DM variations for the SpectralModel fit, and a power-law DM model for the TEMPONEST fit. In both plots, the zero on the y-axis represents the value returned by TEMPO2, with the y-axis being in units of the 1σ TEMPO2 error. Therefore, a fit consistent with that returned by TEMPO2 will have a value of 0 ± 1 in these plots.

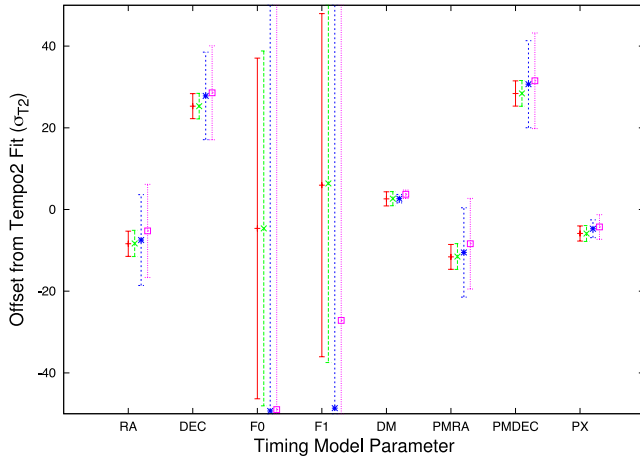
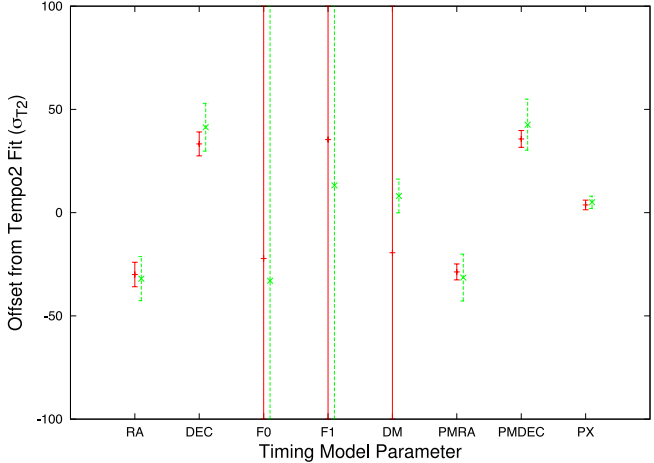


Figure 12. Difference between the timing model parameter estimates returned by TEMPONEST under a series of different approximations and the TEMPO2 parameter estimates in the same format as Fig. 11, as well as the timing model estimates returned by the SpectralModel plug-in for data set 1. For each timing model parameter from left to right the data points represent the following: (i) full analysis using TEMPONEST, (ii) using the linear timing model, linearized at the timing model parameters estimated by the SpectralModel plug-in, (iii) as (ii) but with the EFAC = 1, EQUAD = 0, $\gamma_{\text{red}} = -4.0$ and (iv) the SpectralModel fit.

Fig. 12 shows the timing model parameters estimated from these different approximations in the same format as in Fig. 11. The red and green points represent the parameter estimates from the full non-linear timing analysis, and the linearized analysis, respectively; however, there is no discernible difference in either the estimated parameter values, or the uncertainties between these two models, as expected given the set of parameters included in the timing model. The blue points represent the case where we have not included white noise in the model, and have fixed the spectral index of the red noise to be that used in the SpectralModel analysis (-4.0). Here, there is a clear increase in the level of uncertainty of the timing model parameters relative to the full analysis by a factor of $\sim 2\text{--}3$ except for DM which sees the uncertainties decrease by ~ 60 per cent. In both cases however, this brings the estimated uncertainties in line with those derived from the SpectralModel analysis, with remaining



differences being of the order 10 per cent, with the exception of the quadratic spin-down parameters, from which we would expect the greatest difference given the use of different red noise models.

This clearly emphasizes the importance of including as much as is required to fully describe the data simultaneously in the fit along with the timing model parameters. We should make clear that the magnitude of the differences observed in PSR B1937+21 will not be typical for most MSPs; however, the precise level of difference to expect is difficult to quantify a priori, being a function of signal to noise, the cadence of the observations and the complexity of the timing model used to describe the pulsar. We therefore still suggest that unless a full simultaneous analysis such as that described here is performed in every case, the unpredictable variation in the uncertainties returned from the analysis must impact the robustness of the science extracted from that analysis.

8 CONCLUSION

We have introduced TEMPONEST, a software package that provides a means of performing a robust Bayesian analysis of pulsar timing data. TEMPONEST allows for the joint analysis of the timing model along with a range of additional stochastic parameters including EFAC and EQUAD parameters, and descriptions of both red spin noise and DM variations using either a power-law description of the noise, or in a model-independent way, parametrizing the power at individual frequencies in the data.

We have applied TEMPONEST to both simulated and real data sets in order to demonstrate several key aspects of functionality. First, we used simulated data for the pulsar PSR J1713+0747 in order to compare the linear and non-linear timing models, where the level of noise varied between simulations, from that expected from the square kilometre array (~ 100 ns white timing noise), to a level more representative of current observations, including red spin noise. We showed that in the high signal-to-noise example the differences between the timing solutions for the linear and non-linear timing model parameters were negligible. In the lower signal-to-noise examples, however, the linear timing model failed to capture all the information present in the data, with large curving degeneracies in the non-linear parameter space leading to uncertainties that exceeded those in the linear approximation by up to an order of magnitude.

We then applied TEMPONEST to two publicly available data sets, the binary pulsar B1855+09 and the isolated pulsar B1937+21. For the former, we used a model-independent method of parametrizing the red spin noise in the data and found marginal support for a single low-frequency component in addition to the timing model parameters fitted, but found that it did not affect the timing model solutions in any observable way, with parameter estimates that were completely consistent with those of TEMPO2 in all respects. We then demonstrated the ability for TEMPONEST to perform model selection using the evidence by including a series of additional timing model parameters and repeating the analysis in order to find the optimal set that described the data. This included adding jumps between instrument back ends, and additional physical parameters such as derivatives of the binary period or eccentricity.

In the case of B1937+21, we used both a power-law, and a model-independent method of parametrizing both the DM and red noise signals in the data, and found whilst they gave consistent results, the evidence heavily favoured the use of the simpler model, with both components being well described by a power-law power spectrum with spectral indices of -2.7 ± 0.3 and -5.3 ± 0.9 , respectively. When comparing the timing model solutions returned by TEMPONEST from this joint analysis with those of TEMPO2, we found large discrepancies, both in terms of the parameter estimates themselves and their uncertainties. In the most extreme cases, the TEMPONEST parameter estimates were up to $\sim 38\sigma_{T_2}$ away from the TEMPO2 values, with σ_{T_2} the returned TEMPO2 uncertainty, whilst the uncertainties themselves were over two orders of magnitude greater in the case of the pulsar's spin-down parameters. When compared to the Cholesky method found in the TEMPO2 SpectralModel plug-in, we found that by not including all the stochastic processes in the analysis simultaneously with the timing model, the timing model parameter uncertainties are overestimated by a factor $\sim 2-3$ in almost all cases, showing unambiguously the importance of including as much as is required to fully describe the data simultaneously in the analysis. This is all the more critical given the precise level of difference to expect for any pulsar is difficult to quantify a priori, being a function of signal to noise, the cadence of the observations, and the complexity of the timing model used to describe the pulsar. We therefore suggest that unless a full simultaneous analysis such as that described here is performed in every case, the unpredictable variation in the uncertainties returned from the analysis must impact the robustness of the science extracted from that analysis.

TEMPONEST is freely available as a development build,⁴ with a full public release planned in the near future.

ACKNOWLEDGEMENTS

KJL is supported by the ERC Advanced Grant ‘LEAP’, Grant Agreement Number 227947 (PI Michael Kramer).

⁴ <https://github.com/LindleyLentati/TempoNest>

REFERENCES

- AMI Consortium et al., 2012, preprint ([arXiv:1210.7771](https://arxiv.org/abs/1210.7771))
- Bailes M. et al., 2011, Science, 333, 1717
- Cameron E., Pettitt A., 2013, preprint ([arXiv:1301.6450](https://arxiv.org/abs/1301.6450))
- Coles W., Hobbs G., Champion D. J., Manchester R. N., Verbiest J. P. W., 2011, MNRAS, 418, 561 (C11)
- Demorest P. B. et al., 2013, ApJ, 762, 94
- Edwards R. T., Hobbs G. B., Manchester R. N., 2006, MNRAS, 372, 1549
- Espinosa C. M., Lyne A. G., Stappers B. W., Kramer M., 2011, MNRAS, 414, 1679
- Feroz F., Hobson M. P., 2008, MNRAS, 384, 449
- Feroz F., Hobson M. P., Bridges M., 2009, MNRAS, 398, 1601
- Feroz F., Balan S. T., Hobson M. P., 2011, MNRAS, 415, 3462
- Feroz F., Hobson M. P., Cameron E., Pettitt A. N., 2013, preprint ([arXiv:1306.2144](https://arxiv.org/abs/1306.2144))
- Hobbs G. B., Edwards R. T., Manchester R. N., 2006, MNRAS, 369, 655
- Hobbs G. et al., 2009, MNRAS, 394, 1945
- Hobson M. P., Bridle S. L., Lahav O., 2002, MNRAS, 335, 377
- Jaffe A. H., Backer D. C., 2003, ApJ, 583, 616
- Janssen G. H., Stappers B. W., Kramer M., Purver M., Jessner A., Cognard I., 2008, in Bassa C., Wang Z., Cumming A., Kaspi V. M., eds, AIP Conf. Proc. Vol. 983, 40 Years of Pulsars: Millisecond Pulsars, Magnetars and More. Am. Inst. Phys., New York, p. 633
- Kaspi V. M., 1995, in Hog E., Kenneth Seidelmann P., eds, Proc. IAU Symp. 166, Astronomical and Astrophysical Objectives of Sub-Milliarcsecond Optical: Astrometry. Kluwer, Dordrecht, p. 163
- Kaspi V. M., Taylor J. H., Ryba M. F., 1994, ApJ, 428, 713 (K94)
- Keith M. J. et al., 2013, MNRAS, 429, 2161
- Kramer M. et al., 2006, Science, 314, 97
- Lee K. J., Bassa C. G., Janssen G. H., Karuppusamy R., Kramer M., Smits R., Stappers B. W., 2012, MNRAS, 423, 2642
- Lee K. J. et al., 2013, MNRAS, submitted
- Lentati L., Alexander P., Hobson M. P., Taylor S., Gair J., Balan S. T., van Haasteren R., 2013, Phys. Rev. D, 87, 104021 (L13)
- Liu K., Keane E. F., Lee K. J., Kramer M., Cordes J. M., Purver M. B., 2012, MNRAS, 420, 361
- Lorimer D. R., Kramer M., 2004, Ellis R., Huchra J., Kahn S., Rieke G., Stetson P. B., eds, Handbook of Pulsar Astronomy. Cambridge Univ. Press, Cambridge
- O’Ruanaidh J. J. K., Fitzgerald W. J., 1996, Numerical Bayesian Methods Applied to Signal Processing. Springer-Verlag, New York
- Phinney E. S., 2001, preprint ([astro-ph/0108028](https://arxiv.org/abs/astro-ph/0108028))
- Shannon R. M., Cordes J. M., 2010, ApJ, 725, 1607
- Skilling J., 2004, in Fischer R., Preuss R., von Toussaint U., eds, AIP Conf. Proc. Vol. 735, Bayesian Inference and Maximum Entropy Methods in Science and Engineering. Am. Inst. Phys., New York, p. 395
- Splaver E. M., Nice D. J., Stairs I. H., Lommen A. N., Backer D. C., 2005, ApJ, 620, 405
- Trotta R., 2007, MNRAS, 378, 72
- van Haasteren R., Levin Y., 2013, MNRAS, 428, 1147 (vHL2013)
- van Haasteren R., Levin Y., McDonald P., Lu T., 2009, MNRAS, 395, 1005 (vH2009)